An investigation of the atmospheric wave dynamics in the polar region using ground based instruments

by

Bhekumuzi Sfundo Khanyile

Submitted in fulfilment of the academic requirements for the Degree of Master of Science,
School of Physics, University of Fort Hare

Supervisor: Dr V. Xuza

Co-supervisor: Dr S.B. Malinga

December 2011

Abstract

This study presents the characteristics of small-scale gravity waves in the mesosphere region as derived from the imaging riometer data at high altitude (~90 km) over SANAE (72˚S, 3˚W). Wavelet analysis and FFT (Fast Fourier transform) have been applied to extract short period gravity wave parameters for the year 2000. The horizontal wavelength, phase speed and observed period of gravity waves are typically 10-100 km, 5-60 $m.s^{-1}$ and 3-60 minutes, respectively. The horizontal propagation direction is north-eastward throughout the year. This could probably be due to selective filtering by the zonal wind.

Zonal and meridional winds in the region of the MLT (mesosphere and lower thermosphere) have been measured using HF radars at high latitudes in the southern hemisphere. Data from January 2000 to December 2003 have been used with the aim of investigating the characteristics of planetary wave activity at ~90 km. For SANAE and Halley stations, 2-, 5-, 10-, 16- and 20-day planetary waves are dominant in summer and winter. The results show the seasonal variations of the mean winds, which are caused by the internal variability of the quasi stationary planetary waves.

Planetary wave coupling processes between UKMO assimilated and mesospheric data have also been investigated. The cross wavelet results show a strong coupling during winter months. The results suggest that planetary waves are generated at lower atmospheric heights and propagate upwards into mesospheric heights. However, not all observed disturbances in mesospheric heights can be explained by the propagation of planetary waves from lower atmospheric heights.

Preface

The work described in this thesis was carried by the author at the SANSA (South African National Space Agency), Hermanus, and Department of Physics, University of Fort Hare in the Eastern Cape, from January 2009 to December 2011 under supervision of Drs S.B. Malinga and V. Xuza.

This work represents original work by the author and has not been submitted in any form to any university. The work of others has been duly acknowledged where used in the text.

Bhekumuzi Sfundo Khanyile

Signature:_____ Date:_____

Acknowledgements

The author would like to acknowledge and thank the following for their generous contribution to the success of this thesis, in no particular order:

- My supervisors, Drs S.B. Malinga and V. Xuza for their assistance and guidance provided during the preparation and compilation of the thesis.
- My mentors, N.M. Mbatha, S.H. Mthembu and J. Bosco Habarulema for their valuable assistance.
- The SANSA Space Agency for financial assistance throughout my studies.
- Petro du Preez, for assisting in proofreading and editing.
- My family and friends for their moral support.

Dedication

To my Parents

Table of Contents

Table of figures

Chapter 1 Introduction

1.1 Atmospheric structure

The aim of this study is to investigate the wave dynamics of the middle to upper atmosphere in the polar region. This includes the propagation characteristics of atmospheric waves of various time and spatial scales, as well as their non-linear interactions with one another and the background atmospheric state. Coupling between the neutral and ionospheric atmosphere structures through wave dynamics is also investigated.

The temperature profile structure of the atmosphere changes on many scales of time and space. The clearest scale is the annual cycle, but there are also changes on longer time scales such as the quasibiennial oscillation and interannual variability scales, and on smaller scales such as gravity waves, tides and planetary waves (Grandal & Holtet, 1977). Gravity waves are classified as short and long period waves, depending on their time periods. Gravity waves with intervals of 1-60 minutes are usually taken as short period gravity waves (Moffat-Griffin et al., 2008) while long period gravity waves have intervals of approximately 2-8 hours (Tunbridge and Mitchell, 2009). Similarly, planetary waves are classified into two types, namely, short period waves of less than 10 days and long period waves of longer than 10 days (Kishore et al., 2004; Malinga and Ruohoniemi, 2007; Pancheva et al. 2008, 2009).

Generally, the earth's atmosphere consists of gases such as argon (Ar), nitrogen (N_2), oxygen (O_2), carbon dioxide (CO_2), ozone (O_3), water vapour (H_2O), ammonia (NH_3) and methane (CH_4) (Grandal and Holtet, 1977; Kato, 1980; Andrews, 1987). The earth's atmosphere is a region of pressure, density and temperature change with height, and is held in place by the gravitational force in the hydrostatic equilibrium of the planet (Kato, 1980; Andrews, 1987). The hydrostatic equilibrium is the balancing of the vertical pressure gradient and the gravitational force per unit volume acting on each portion of the atmosphere (Andrews, 1987).

Fig. 1.1 shows a typical temperature profile of up to about 120 km. The earth's atmosphere is roughly classified into four regions, namely, the troposphere (from ground to 15 km), the stratosphere (15-50 km), the mesosphere (50-80 km) and the thermosphere (80-100 km). These regions have different characteristics and compositions and therefore varying thermodynamics. The regions are delineated by rapid change in temperature gradients. In this study, the focus is on the stratosphere and mesosphere regions, also known as the lower and middle atmosphere.

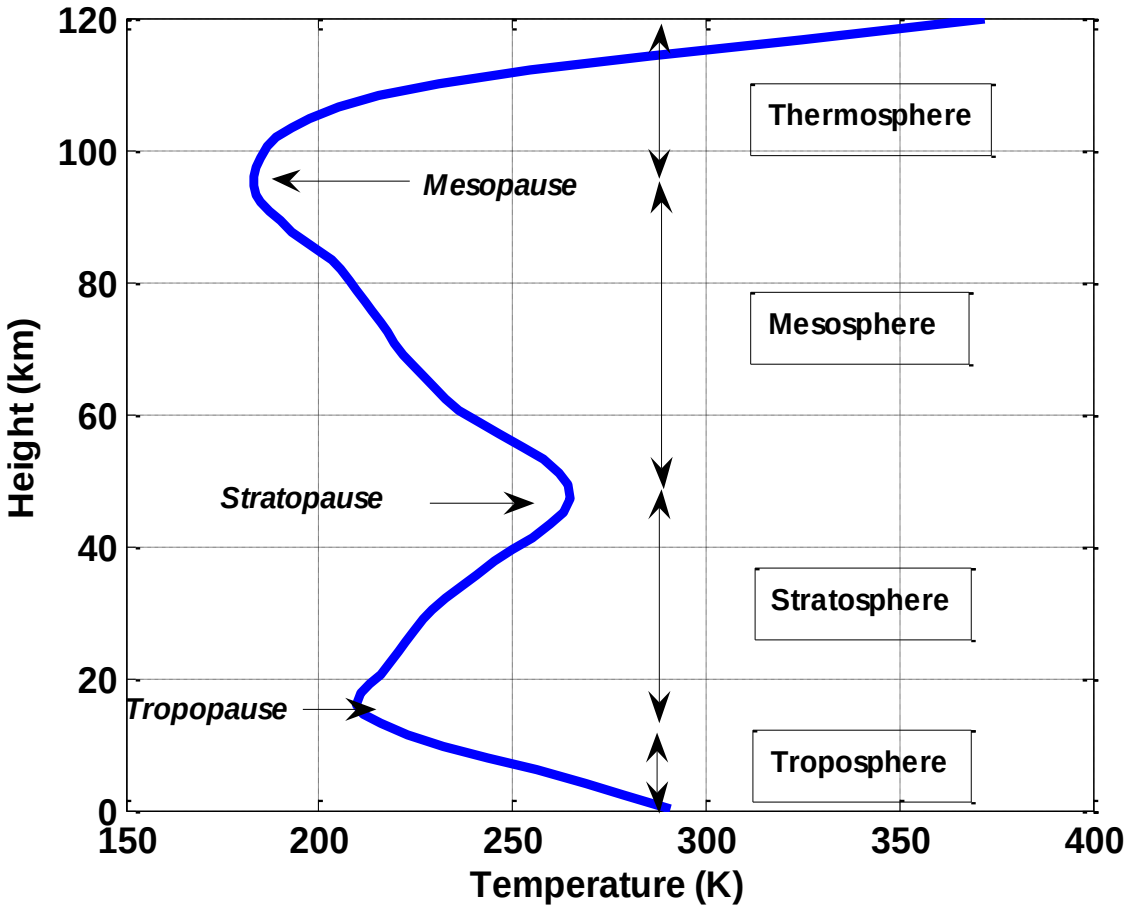

Figure. 1.1. The vertical structure of atmospheric temperature up to about 120 km altitude.

The troposphere is known for a decrease in temperature and the stratosphere for an increase in temperature. In the troposphere, the temperature distribution is maintained by a convective and turbulent transfer of heat due to the absorption of the solar radiation at the surface (Grandal and

Holtet, 1977). Most of the terrestrial weather phenomena such as cyclones, storms, convection, winds systems, fronts hurricanes, snow, thunder and lightning occur in the troposphere.

The stratosphere contains ozone molecules which are produced through photochemical processes involving the absorption of solar ultraviolet photons by molecular oxygen. The equilibrium profile of the ozone depends on chemical ozone destruction processes and on the transport of the ozone by winds (Andrews, 1987). The ultraviolet light interacting with the ozone causes a rise in temperature. The ozone layer is thermally stratified in temperature with dense, cooler air below the warmer and lighter layers. The reason the temperature increases with altitude is that most ozone molecules are contained in the stratosphere (Grandal and Holtet, 1977).

Above the stratosphere is the mesosphere (sometimes called the middle layer), where the temperature decreases with height. In this region, the air is extremely thin and the atmospheric pressure is quite low. Although the percentage of nitrogen and oxygen in the mesosphere is about the same as at the earth's surface, a breath of mesospheric air contains far fewer oxygen molecules than a breath of tropospheric air.

The layer above the mesopause (the end layer of the mesosphere) is called the thermosphere or warmer layer, where temperature increases with altitude. The number of molecules present is few, energetic, and has low density (Andrews, 1987).

The mesosphere and thermosphere are sometimes jointly called the ionosphere, because at this height, most of the molecules and atoms are ionised by ultraviolet light and high energy particles. Most radio signals rebound in this region, playing a major role in radio communications. The D region reflects standard AM (amplitude modulation) radio waves back to earth, but at the same time seriously weakens them through absorption (Andrews, 1987).

Air molecules are held near the earth by the force of gravity. Since air density is the number of air molecules in a given volume, it follows that air density is greatest at the surface and decreases as move up into the atmosphere. Air molecules have weight, the weight of the air molecules acts as a force upon the earth. The amount of force exerted over an area of surface is called

atmospheric pressure. The pressure at any level in the atmosphere the pressure may be measured in terms of the total mass of the air above any point (Grandal and Holtet, 1977).

The thermal structure of the atmosphere is affected by the vertical distribution of the solar and thermal radiative energy deposition; the magnitude of the internal heat source; the dynamic response of the atmosphere to the various energy sources; thermal radiation and convection energy transported; the absorption and emission of solar radiation, and the large scale thermal structure of the planetary atmosphere (Shirley and Fairbridge, 1997).

Other factors which affect the atmospheric thermal structure include clouds and infrared emission by water vapour, both of which are mainly responsible for the temperature minimum in the tropopause or top layer of the troposphere. The temperature peak of the stratospause or end layer of the stratosphere is due to the absorption of solar ultraviolet radiation by ozone, whereas the temperature minimum at the mesopause is primarily due to a large decrease in ozone concentration at that level, which greatly reduces solar absorption (Andrews, 1987). The decrease in temperature radiation into the ground causes the temperature profile to be statically unstable. This, in turn, gives rise to convective activity that modifies temperature distribution, causing it to decrease less quickly with height until it reaches a statically stable state again (Andrews, 1987). Midlatitude cyclones and anticyclones play an essential role in determining the temperature structure at higher latitudes (Andrews, 1987).

1.2 Project Objectives

The main objective of this project is to investigate whether the SANAE imaging riometer can be used to study short period gravity waves (3-60 minutes). While similar studies were undertaken before (Jarvis et al., 2003; Moffat-Griffin et al., 2008) using a similar instrument over Halley (76°S, 27°W), prior to this study the data collected from the imaging riometer over SANAE had not been analysed with the purpose of identifying gravity waves. Although, imaging riometer is an advanced riometer which uses a narrow beam antenna array to spatially sample the region of interest, it is used for ionospheric studies such as precipitation (Wilson, 2000). Wave parameters analysed using the imaging riometer includes the horizontal wavelength, the horizontal phase velocity and horizontal propagation direction.

In this study, HF (high frequency) radar and UKMO (United Kingdom Met Office) assimilated data are used to investigate planetary waves coupling processes in the middle atmosphere. HF radar is a powerful instrument that is used to study the behaviour of the earth's ionosphere, especially ionospheric irregularities in the D region. These data sources were previously used to study a quasi-two-day wave in the Northern Hemisphere (Malinga and Ruohoniemi, 2007) and planetary wave coupling processes in the middle atmosphere (Chshyolkova et al., 2006 and Pancheva et al., 2009). The analysis techniques employed include various signal processing routines such as wavelet analysis and FFT (Fast Fourier technique).

The results of this study will enhance the understanding of gravity wave momentum and energy deposition in the middle atmosphere. Gravity waves attain large amplitudes in this region and as they propagate upward, their amplitudes increase further. This is because the atmospheric density decreases with increasing altitude. At the maximum amplitude they tend to break and deposit momentum and energy into the mean circulation (Oleynikov et al., 2005, 2007; Espy et al., 2004). These breaking gravity waves may cause the wind to reverse in the mesosphere and lower thermosphere (MLT) regions and in the process allow for the upward propagation of planetary waves.

1.3 Thesis overview

The thesis consists of seven chapters. In chapter one, the background atmosphere, project objectives and thesis overview are discussed. Chapter two presents a literature review of the atmospheric waves, while chapter three gives a brief description of instruments and data analysis techniques. A full investigation of the propagation conditions of atmospheric waves along with the corresponding assimilation results from UKMO model and high frequency radars are presented in chapters' four to six. Finally, the main results are summarised in chapter seven.

Chapter 2 Atmospheric waves

2.1 Introduction

This chapter focuses on three types of atmospheric waves, namely, gravity waves, tides and planetary waves. They have different periods, lasting from a few minutes to days. For example, gravity waves have periods of a few minutes to several hours e.g. ~3 minutes to 6 hours, tides can last from ~8-24 hours and planetary waves usually last ~2-30 days and upwards.

Many instruments have been used to study these waves, including high frequency (HF) radars and satellites, but in this study the focus will be on high frequency radars and imaging riometer instruments. Briefly, this study will present a basic understanding as well as work done by other experts. Neither a detailed theory of gravity waves nor a mathematical model of linear gravity waves will be presented. Such exposition can be found elsewhere (McLandress, 2001; Kshevetskii and Gavrilov, 2005; Jacobi et al., 2006, Sun et al., 2007; Zhu, 2007). In this thesis the focus is on the experimental analysis of atmospheric waves.

2.2 Gravity waves

Gravity waves owe their existence to buoyancy restoring forces, while inertia gravity waves are due to the combined effects of the buoyancy restoring force and Coriolis force. Gravity waves are generated in many different ways, including air flow over mountains; geotropic generation; convective activity in the troposphere; cumulus clouds and thunderstorms; atmospheric fronts and the frontal jet; orography; shear instability; volcanoes; earthquakes; ground level explosions; shear flows; burning down satellites, and big fires (Andrews, 1987; Vincent and Alexander, 2000; Fritts and Alexander, 2003; Kshevetskii and Gavrilov, 2005; Bageston et al., 2009).

Gravity waves play an important role in the mean circulation, temperature structure and global scale circulation of the atmosphere (Andrew, 1987; Moffat-Griffin et al., 2008; Dou et al., 2010; Pragati et al., 2010; Mitchell and Beldon, 2009). Atmospheric wave motions are the driving force

of the mean circulation and thermal structure of the MLT region via wave energy and momentum transport (Medeiros et al., 2002; Moffat-Griffin et al., 2008; Suzuki et al., 2009).

Waves generated in the lower atmosphere might propagate upwards into the stratosphere and mesosphere. As the background air density decreases, the amplitude of the wave fluctuations in the wind rises. As a result, the gravity waves may attain large amplitudes; they may consequently break and deposit momentum and energy into the mean circulation (Vincent and Alexander, 2000; Oleynikov et al., 2005; Espy et al., 2004). These breaking gravity waves sometimes cause the wind to reverse in the MLT region and open up for the upward propagating planetary waves. Consequently, gravity waves control the thermal balance in the MLT region through wave dissipation and the accompanying momentum flux divergence (Fritts and Alexander, 2003).

Depending upon the filtering action of the winds below, this input of momentum closes the mesospheric jets and limits wind speeds while driving the mesopause winds and temperatures far from radiative equilibrium. Because of middle atmospheric filtering processes, gravity waves with phase speeds of less than the magnitude of the jet velocity are only able to reach the mesopause region if they propagate opposite to the mean wind direction (Espy and Stegman, 2002; Fritts and Alexander, 2003).

Medeiros et al. (2003) observed a tendency for short period gravity waves to propagate in a northward direction in the northern hemisphere during the summer months (May, June, and July). Their study explains the preferential direction of gravity waves as a result of critical filtering, which is caused by the interaction between the upward propagating waves and the horizontal mean flow background. Moreover, the horizontal propagation directions of gravity waves show a clear seasonal dependence, as the propagation direction is greatly influenced by the background atmospheric condition in the propagation paths and the locations of the wave sources (Suzuki et al., 2004, 2009; Dietrich et al., 2005; Nielsen et al., 2009).

Short period gravity waves (typically a few minutes to several hours) with a wavelength of a few kilometers to a few hundred kilometers studied in the MLT region, using OH airglow (Nakamura et al., 1999, 2001, 2003; Jarvis et al., 2003; Medeiros et al., 2002, 2003, 2004, 2005, 2007;

Moffat-Griffin et al., 2008). In fact, most authors have reported short period wave-like oscillations evident in the visible and near infrared airglow layers. These oscillations are divided into two categories, namely, bands and ripples.

Bands have a long period or distance, tend to have long horizontal wavelengths and speeds of less than 100 $m.s^{-1}$, and can transport momentum (Jarvis et al., 2003; Medeiros et al., 2002, 2003, 2005; Moffat-Griffin et al., 2008, Pragati et al., 2010). Ripples, on the other hand, are short-lived scale waves that are generated by localised shear or convective type instabilities (Shiokawa et al., 2002, 2009) and wave-to-wave interaction in the total wind field (Pragati et al., 2010).

Recently, several attempts were made to calculate gravity waves parameters using an imaging riometers. This instrument is capable of detecting short period mesospheric gravity waves using fluctuations of the ionospheric absorption of cosmic radio noise tracer. Jarvis et al. (2003) and Moffat-Griffin et al. (2008) used the imaging riometer and compared it with imager airglow to study the gravity wave activity in the mesosphere region. Their aim was to understand the horizontal wave parameters and propagation direction of the short period gravity waves. The results of the airglow imager and imaging riometer showed good agreement between the two instruments.

2.3 Tides waves

The term atmospheric tides refer to those oscillations in any atmospheric field whose periods are integral fractions of either a lunar or a solar day (diurnal, ~24h; semidiurnal, ~12h; and terdiurnal, ~8h). Atmospheric tides are not only excited by the tidal gravitational potential of the sun and moon, but also by variations in solar heating. There are two possible forcing functions for tidal waves, gravitational forces and the diurnal variations of heating (thermal forcing). This tidal excitation responds to the atmosphere by means of internal gravity waves. Atmospheric tides are studied to understand their frequencies and zonal wavenumbers, the magnitude and distribution of their excitation, and because they form a substantial part of the total meteorology of the upper atmosphere. Strong wind oscillations are associated with the upward propagation tidal modes that are excited in the troposphere and stratosphere (Grandal and Holtel, 1997).

Solar semidiurnal tides are defined as the dominant atmospheric pressure variation in the tropics. These tides have the greatest amplitudes and are influenced by the large pressure changes associated with mid latitude planetary scale disturbances. The pressure maximum of a solar semidiurnal tide is observed to occur 2-3 hours before local noon and midnight. The amplitude of the pressure varies near the equator. These tides are mostly stationary waves making a minor contribution at low latitudes but dominating at high latitudes. Semidiurnal tides are hardly affected by seasons. However, local irregularities due to the earth's topography affect the phase of the semidiurnal tides (Tom Beer, 1974). Generally, semidiurnal tidal oscillations at the tropics are stronger than the same tides at mid latitudes, and they have an unusual seasonal variation in a phase that occurs in both the northern and southern hemispheres (Tom Beer, 1974).

Diurnal oscillation is the primary harmonic oscillation of the solar daily cycle and is capable of upward propagation at low latitudes. According to the classical linear theory, in the absence of dissipation, diurnal tidal amplitude will grow exponentially with height in response to the decrease of atmospheric density. This suggests that small scale gravity waves originating in the lower atmosphere can also propagate upward and reach substantial amplitude in the atmosphere (Akmaev, 2001). In the MLT region, diurnal tides feature prominently and have significant migrating and non-migrating components. Migrating diurnal tides have strong seasonal variation, reaching large amplitudes during the equinoxes and having smaller values during solstices (Wu et al., 2008; Tom Beer, 1974). Moreover, ground based observations have revealed many important features of the diurnal tide such as seasonal and interannual variations of the MLT diurnal tide (dominant in the subtropics) at various latitudes (Akmaev, 2001; Smith, 2000; Wu et al., 2008).

Most studies conducted for the MLT region have shown that terdiurnal atmospheric tides are likely to be observed in this region. For instance, radars indicated that the terdiurnal tide often feature in the MLT region. The radars showed the horizontal winds (zonal and meridional) variability in the region and the amplitudes varying with the seasons, particularly showing strong amplitudes in winter. Sometimes, the terdiurnal tide amplitudes can be as large as the diurnal and semidiurnal tides in the mid latitudes (Smith, 2000; Smith and Ortland, 2000).

In summary, tides play an important role in the mesosphere and lower thermosphere, as they transport momentum and wave energy upward and then dissipate through various instabilities and nonlinear wave interactions. The large migrating tides are a response to the absorption of solar radiation by water vapour in the troposphere, the ozone in the stratosphere and mesosphere, and molecular oxygen in the lower thermosphere. The impact of tides on the temperature, wind, and density structure is also significant in the MLT region. These parameters are influenced by the solar forcing as well as by propagating tides originating in the troposphere and stratosphere (Smith, 2000).

2.4 Planetary waves

Atmospheric waves (planetary waves, thermal tides and gravity waves) with different spatial and temporal scales play an important role in the dynamic behaviour of the middle atmosphere. An example of the planetary waves that are prominent in the MLT is the quasi 2-day wave. Its characteristics have been widely studied and mostly has a westward wave number 3 (Lima et al., 2004; Malinga and Ruohoniemi, 2007; Tunbridge and Mitchell, 2009).

The quasi 2-day wave is observed around summer solstice every year. The wind speed measured can reach values of up to 50 $m.s^{-1}$ during the southern hemisphere summer, while the northern hemisphere values are usually lower (30-50 $m.s^{-1}$) for the meridional component. The wave is westward propagating with a predominantly zonal wavenumber 3, although zonal wavenumbers 2 and 4 have also been observed. The period of the wave ranges from 43 to 55 hours with larger frequency variations in July and August in the Northern hemisphere (Rojas and Norton, 2007).

There are two theories attempting to explain the source of the quasi 2-day wave. Firstly, the wave is a zonal wavenumber 3 Rossby gravity normal mode. This is a (3, 0) mode in the solution of Laplace's tidal equation. The (3, 0) Rossby gravity mode for an isothermal atmosphere at rest has a period of ~50 hours. The second theory is that the quasi 2-day wave is caused by the baroclinic instability of the summer jet. For example, Rojas and Norton (2007) studied the source of the quasi 2-day wave and suggested that it was caused by the baroclinic instabilities in the summer substropics near the stratospause.

Planetary waves have been extensively studied by ground based radars, for instance HF radar, meteor and MF (medium frequency) radars, and have been used to investigate the climatology of wave activity at middle and low altitudes (Jacobi et al., 2006; Tunbridge and Mitchell, 2009). The global scale structure has been investigated using satellite data (Riggin et al., 2004; Pancheva et al., 2008). Theoretical studies have investigated the excitation of these waves, their global structure and their interaction with other waves and tides (Salby and Callaghan, 2000).

The dynamics of the middle atmosphere in winter are known to be dominated by planetary waves of large amplitudes, especially quasi stationary Rossby waves. These waves propagate upward from the stratosphere and are very strong but quite variable during winter. Other planetary waves are the travelling normal modes, also known as free modes. These are the commonly observed modes with periods of around 2, 5, 10 and 16 days. Free modes do not transport much momentum but can interact with other waves or the zonal mean flow. This process is called wave-wave interaction. It plays an important role in the dynamics of the middle atmosphere and certainly contributes significantly to the variability of the population of atmospheric waves at these heights (Pancheva et al., 2008, 2009).

The interaction between planetary waves and the zonal mean flow is known to be the major driver of winter stratospheric dynamics (Andrews, 1987). Classical studies showed that the zonal mean flow affects planetary wave propagation by changing the refractive index (Charney and Drazin, 1961). Dissipating planetary waves interacting with the zonal mean flow causes SSW (sudden stratospheric warmings).

During the eastward winter winds in the stratosphere-mesosphere system, downward circulation causes adiabatic heating in the stratosphere whereas upward circulation results in adiabatic cooling in the mesosphere (Liu and Roble, 2005; Coy et al., 2005; Pancheva et al., 2008, 2009). In the middle atmosphere, the time period prior to the onset of a SSW is usually characterised by enhanced wave activity during which more than one type of planetary waves may be present i.e. quasi-stationary Rossby waves, zonally symmetric and travelling normal modes. Jacobi et al. (2003); Espy et al. (2005); Palo et al. (2005) and Chshyolkova et al. (2006) have shown that wave forcing is the preconditioning of the atmosphere prior to the SSW.

Planetary waves coupling between the stratosphere and the mesosphere has been studied by many authors (Thompson et al., 2004; Liu and Roble, 2005; Pancheva et al., 2008, 2009). They have observed the variability in the MLT region as the result of the upward propagation of disturbances from the stratosphere, particularly during winter. Dowdy et al. (2004) studied the mesosphere planetary wave activity during the Southern Hemisphere (SH) major SSW in the winter of 2002 and found the presence of a travelling 14-day wave propagating with zonal wave number 1.

Chshyolkova et al. (2006) utilised UKMO assimilated data together with mesospheric winds MF radars. Their aim was to investigating the vertical and latitudinal coupling processes due to planetary waves for December 2000 to December 2002. They found a strong 14-day planetary wave during the austral winter of 2002. Chshyolkova et al. (2006) suggested that this oscillation was generated at the stratosphere and propagated upward into the MLT.

Chapter 3 Instruments and data analysis techniques

3.1 Introduction

In this chapter the instruments and data analysis techniques used in this work will be discussed. Both instruments (the imaging riometer and HF radar) are based in Antarctica. The assimilated United Kingdom Met Office (UKMO) data will also be explained briefly.

Data analysis techniques such as FFT (Fast Fourier Transformer), wavelet analysis, CDS (Cross-Density Spectra) and bandpass filter will be discussed. FFT is a powerful technique for determining frequency content of a signal, but it fails to provide the time of occurrence and the time evolution spectra (Mthembu, 2006). Wavelet analysis will be employed to give the time of occurrence while CDS will be used in determining the common spectrum components. Bandpass filter acts to remove noise in the data.

3.2 Observational data

3.2.1 Imaging Riometer

The imaging riometer at SANAE station is based on the design by Detrick and Rosenberg (1990), which has a 64-elements imaging riometer. This instrument was built by the department of physics (electronic division) at North West (Potchefstroom) University, South Africa. The imaging riometer utilises narrow beam antenna arrays to spatially sample the region of interest as opposed to a spatially isolated measurement from a single wide beam (Moffat-Griffin et al., 2008).

Riometers measure the intensity of cosmic radio noise received at the surface of the earth (Moffat-Griffin et al., 2008). They are used to measure enhancement of the D region ionosphere by energetic charged particles precipitation driven by magnetospheric electrodynamics (Stauning, 1984; Jarvis et al., 2003). Radio noise suffers absorption as it propagates through the

atmosphere to the earth surface. The radio wave excites the ionized plasma of the ionosphere, which loses energy by colliding with the neutral air (Jarvis et al., 2003).

The operating frequencies of the SANAE imaging riometer range between 28 and 40 MHz. Within this operating frequency region, electron and neutral densities are at a maximum. If there is absorption in the atmosphere, the intensity of the cosmic radio noise received at the earth's surface decreases, therefore absorption can be determined. On the other hand, if no absorption occurs, the intensity of the cosmic radio signal received at the earth surface is cyclic, with the period of a sidereal day. This signal is known as a quiet day curve (Jarvis et al., 2003). See Fig. 3.1 for a typical example of the quiet day curves (particularly beam 37) recorded on day 35 in the year 2000.

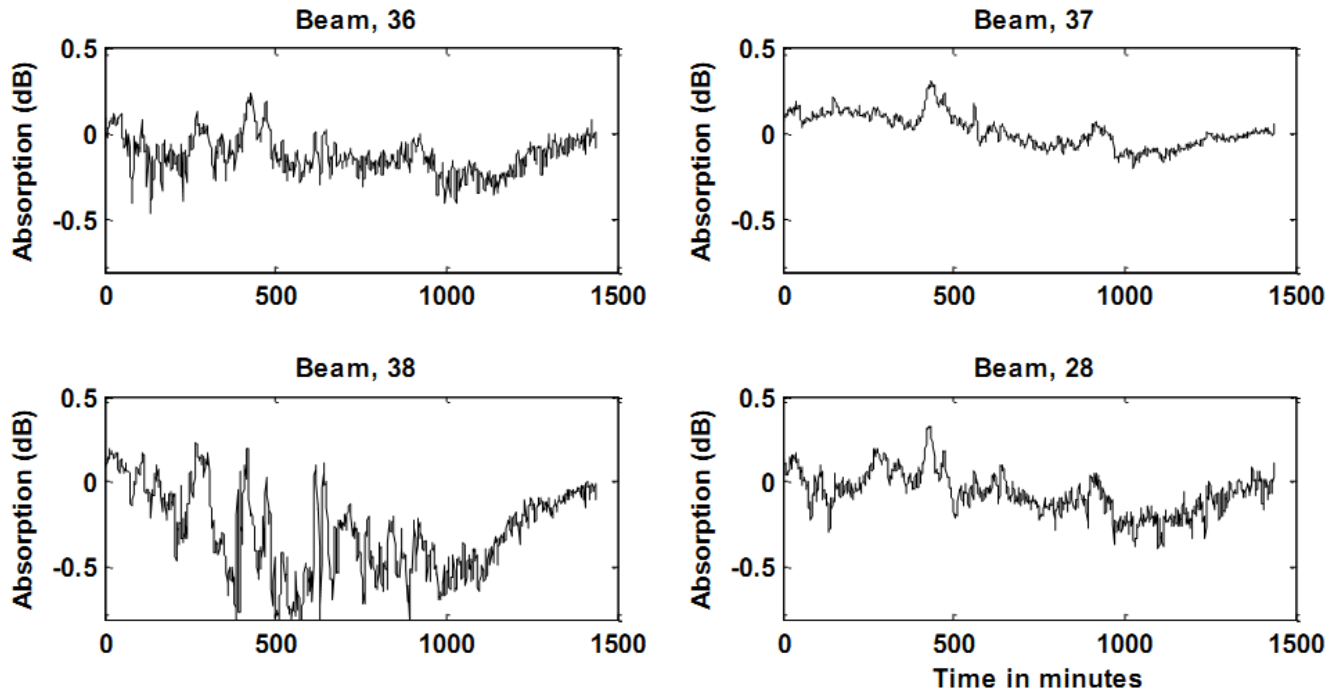

Figure 3.1. A quiet day curves of beams 36, 37, 38 and 28. These beams are diurnal absorption curves recorded on day 35 in year 2000.

The imaging riometer for ionospheric studies (IRIS) at SANAE in Antarctica has a 64 elements crossed dipole arrays, phased to produce 49 separate beams. The operating frequency is 38.2 MHz. The 64 independent beams with a 13˚ degree width cover an area of 200 km^2 at an altitude of ~90 km above the Earth. Riometers record data every 1 s. Fig. 3.2 (a) shows the projection of the imaging riometer beams at ~90 km altitude as the 3dB beam projects, while Fig. 3.2 (b) exhibits the imaging riometer beams at the ground surface at SANAE, Antarctica. The antenna structure in Fig. 3.2 (b) consists of metal pipes and a wire mesh, which provides as electrical ground planes.

(a)

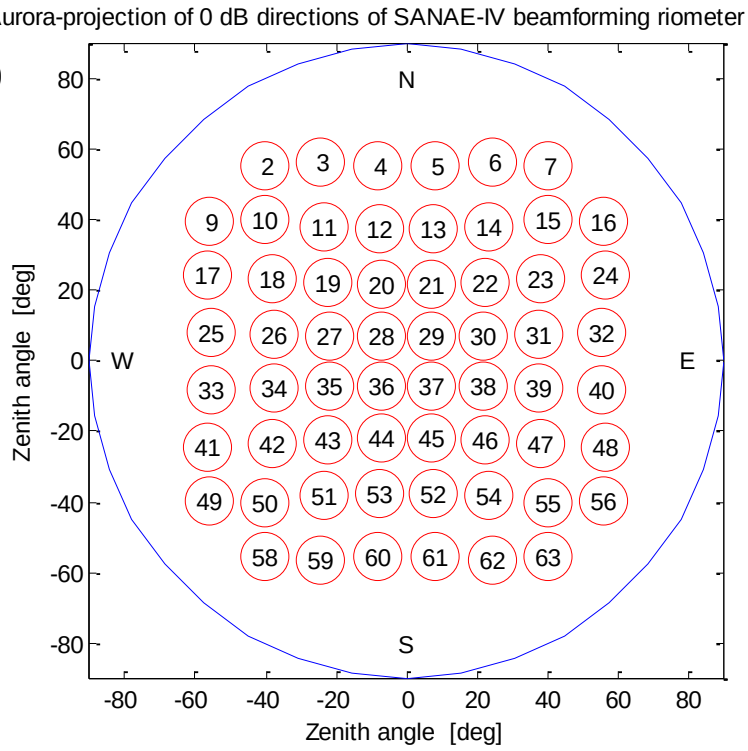

(b)

Figure 3.2. (a) The projection of the imaging riometer beams onto a horizontal plane at ~90 km altitude. (b) The imaging riometer viewed at the earth surface. The ground plane and wire mesh can be seen.

Table 3.1 shows the summarised specifications of the IRIS. The distance beam separation between the circular beam projections near the center is about 22 km while those near the corners form a distorted ellipse and are significantly larger (Jarvis et al., 2003; Moffat-Griffin et al., 2008). The details of the imaging riometer at SANAE are explained in Wilson (2000). The author calculated the directions of the maxima derivatives for the north-west quadrant. Table 3.2 shows some calculated zenith and azimuth angles.

Table 3.1. The summarised specifications of imaging riometer for ionospheric studies.

Parameters	**Values**
Operating frequency	38.2 MHz
Antenna	64-element phased array
Phasing system	49 beam Butler matrix
Beam width	13˚ full -3 dB
Viewing area	200 km square at 90 km height
Resolution	20 km (overhead beam)
Image rate	1 s^{-1}
Sensitivity	0.05 dB

Table 3.2. The 16-beams directions in the north-west quadrant.

Beams	Zenith angle	Azimuth angle
1	N/A	N/A
2	68.60˚	35.57˚
3	61.52˚	23.25˚
4	56.19˚	8.25˚
9	68.60˚	54.43˚
10	56.60˚	45.00˚
11	44.82˚	31.19˚
12	38.15˚	11.47˚
17	61.52˚	66.76˚
18	44.82˚	58.82˚
19	31.57˚	45.00˚
20	22.89˚	18.43˚
25	56.19˚	81.75˚
26	38.15˚	78.53˚
27	22.89˚	71.57˚
28	9.81˚	45.00˚

3.2.2 Data acquisition

The operation of the riometer is controlled by a computer situated at the SANAE base. Every 1/8 of a second, voltage signals are received from the eight by eight riometers and these signals are changed to frequency signals. This happens through a conversion factor of 1V/10kHz. Signals are transmitted by coaxial cables to the processing laboratory inside the base.

The GPS (Global Positioning System) clock is employed for time accuracy. The output signals of all 64 beams are sampled in a one second interval. A file is written every hour containing these 1 Hz values. This creates a file that contains a one-minute value by averaging 60 seconds of sampled data. The digital data is then kept on CD.

3.2.3 Data processing

A file is created to store daily imaging riometer data. Each beam contains its own data set. This applies to all 64 beams. Fig. 3.3 shows the signal beams arrangements on the computer. One beam panel corresponds to a 1 day (24 hrs) curve. These signals are called the diurnal curves.

Wilson (2000) suggested that filters could be used to remove the noise present in the imaging riometer data. Some of these filters are described in the next section. The largest noise factor in SANAE is wind, especially in winter. Other factors that contribute to the noise are the instruments around the base and sometimes even the white noise from the instruments play a role.

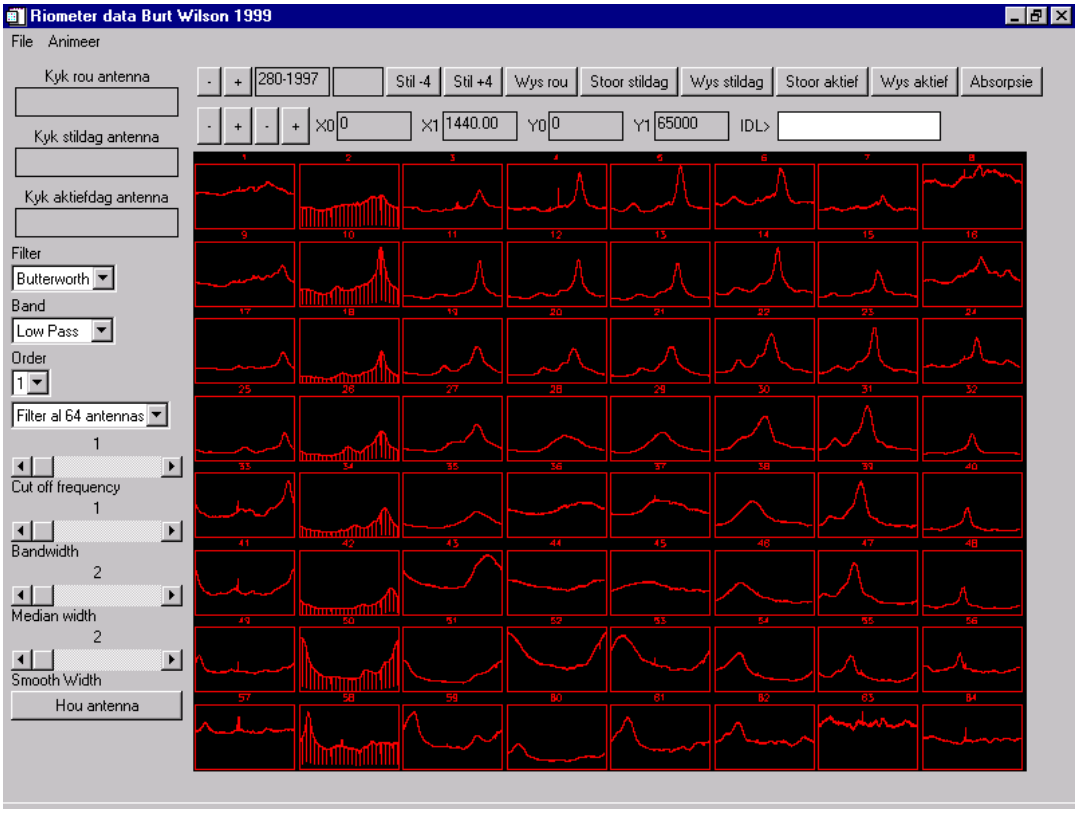

Figure 3.3. A photo of 64 beams data processing (Wilson (2000)).

3.2.4 The SuperDARN HF radar (SANAE)

The SANAE HF radar is part of the SuperDARN HF radar network and is positioned in Antarctica (72˚S, 3˚W). The SuperDARN HF radar was designed to monitor plasma convection in the Northern and Southern high latitude ionosphere. The operating principle of SuperDARN is fully described in Greenwald et al. (1995).

The radar is capable of transmitting signals to the atmosphere and receiving reflected signals from ionospheric irregularities in the E and F regions of the high latitude ionosphere (Greenwald et al., 1995). The SuperDARN HF radar operates within the frequency range of 8-20 MHz. This radar consists of 16 log periodic antennas which form a fan of narrow azimuth of approximately 4˚ with an angular separation of 3.2˚ degrees, which is directed approximately polewards (Jenkins and Jarvis, 1999).

Data are acquired in 2 min scans and all start at even minutes. The peak power is 10 kW and a pulse width of 200-300 microseconds gives a range resolution of 30-45 km. The first range gate is set on 180 km and a range gate of 45 km is used over 75 range cells (Hayashi et al., 2010). In a standard SuperDARN analysis, the backscattered power, the Doppler velocity and the spectral width of the echo spectrum are obtained by fitting a Gaussian and Lorentzian spectral shape to the autocorrelation function from each gate cell of each beam (Greenwald et al., 1995). The viewing field of the northern and southern HF radar is shown in the Figs. 3.4 (a) and (b). Fig. 3.4 (a) shows the antenna array of the HF radar at SANAE, Antarctica while Fig. 3.4 (b) shows the view in the northern (left) and southern (right) hemispheres.

The HF radar instrument has been used to study neutral winds, planetary waves, tides and sometimes gravity waves (Jenkins & Jarvis, 1999). In addition, Malinga and Ruohoniemi (2007) studied the quasi 2-day wave using the northern hemisphere SuperDARN HF radars. In this work, the zonal and meridional wind components from SuperDARN were used to study the dynamics of the MLT region.

(a)

N **S**

(b)

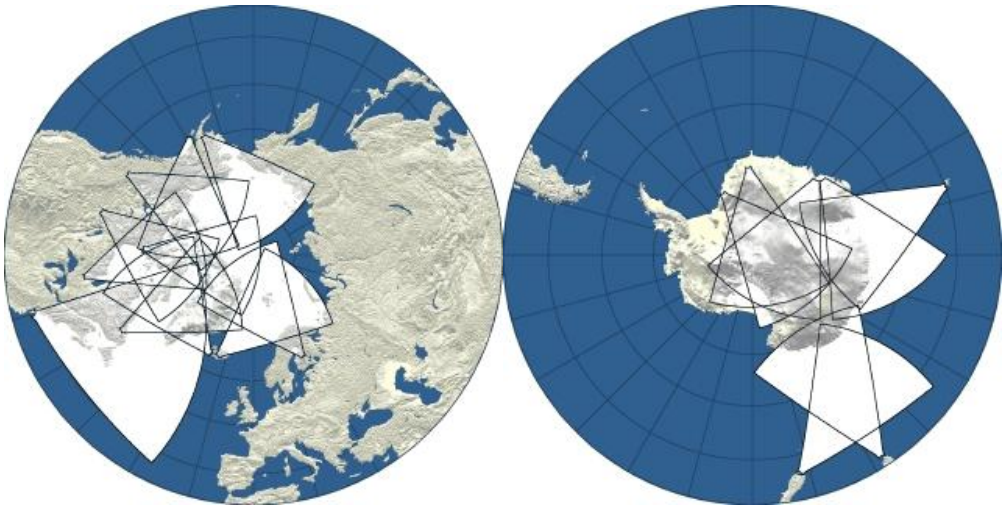

Figure 3.4. (a) The view of the antenna array of the HF radar base located at SANAE. (b) SuperDARN HF radar field of view in the northern (N) and southern (S) hemispheres, respectively.

3.2.5 Assimilated data (UKMO)

The UKMO data assimilation system is an outcome of assimilation of in situ and remotely sensed data into a numerical forecast model of the stratosphere and troposphere (Swinbank and O'Neill, 1994). At pressure levels from 1000 to 0.1 hPa, the outputs of the assimilation are global fields of daily temperature, geopotential height, and wind components (meridional and zonal). The assimilation system uses a global 42-level configuration of the Unified Mode with a horizontal resolution of 2.5˚ and 3.75˚ steps in the latitude and longitude, respectively. It has been running daily since October 1991 to produce near real time global stratosphere analyses at 12 UTC (universal time).

Swinbank and O'Neill (1994) described the original data assimilation system. Lorenc et al. (2000) and Swinbank and Ortland (2003) improved on the data assimilation system and worked with a three dimensional variation data assimilation system which is the updated version. In this study, UKMO data will be used to examine the observations existing in the troposphere and stratosphere. In another example, UKMO assimilated data was used to study planetary waves in the stratosphere by Pancheva et al. (2008). The author studied the vertical coupling of the stratosphere-mesosphere system through quasi-stationary and travelling planetary waves during the major sudden stratospheric warming in the Arctic winter of 2003/2004. UKMO assimilated data were also used to examine the features of the global-scale planetary disturbances present in the winter stratosphere of the Northern Hemisphere.

3.3 Data analysis techniques

3.3.1 Wavelet analysis

Wavelet analysis has been used to study non-stationary time series. WT (wavelet transform) is a technique for analysing non-stationary signals. In addition, it has been used to analyse time series which contain non-stationary power at many different frequencies (Torrence and Compo, 1998). It decomposes signals using a dilated and translated wavelet. The translation represents time, whereas the scale is a way of viewing frequency components.

WT was expanded as an alternative to the STFT (short time Fourier transform) to overcome problems related to its frequency and time resolution properties. Wavelet analysis has been useful in many applications such as transient signal analysis, image analysis and communications systems.

3.3.2 Wavelet transform

Consider a real or complex-value continuous time function $\psi(t)$ with the following conditions:

1. The function integrates to zero:

$$\int_{-\infty}^{+\infty} \psi(t) dt = 0$$

Equation 3.1

2. It is square integrable or, equally, has finite energy:

$$\int_{-\infty}^{+\infty} |\psi(t)|^2 dt \prec \infty$$

Equation 3.2.

The function $\psi(t)$ is a mother wavelet if the two above mentioned conditions and admissibility properties are met. The first condition is suggestive of a function that is oscillatory or that has a wavy appearance, and the second condition implies that most of the energy in $\psi(t)$ is confined to a finite duration (Chui, 1992).

In this work, the mother wavelet used is called a Morlet wavelet. A Morlet wavelet consists of a plane wave complex exponential modulate (Kumar, 1997),

$$\psi(t) = e^{i\omega_o \frac{t}{s}} e^{-\frac{t^2}{(2s)^2}}$$

Equation 3.3

where t is time, s is the wavelet scale, and ω_0 is a non-dimensional frequency. A Morlet wavelet provides a good balance between time and frequency localisation, and serves to extract information about the amplitude and phase of the process investigated.

There are two types of wavelet analysis: CWT (continuous wavelet transform) and DWT (discrete wavelet transform). CTW is best for feature extraction purposes, while DWT is useful for noise reduction and data compression. The CWT holds the capability to build a time-frequency of a signal that offers very good time and frequency localisation (Roberts and Mullis, 1987).

3.3.3 The CWT

The CWT is a function with zero mean. It is localised in both frequency and time. Let $f(t)$ be any square integrable function. The CWT of $f(t)$ with respect to a wavelet $\psi(t)$ is defined as the integral transform

$$wf(u,s) = \int_{-\infty}^{\infty} f(t) \frac{1}{\sqrt{s}} \psi^* \left(\frac{t-u}{s} \right) dt$$

Equation 3.1

where

$$\hat{\psi}_{u,s}(t) \equiv \frac{1}{\sqrt{s}} \hat{\psi}^* \left(\frac{t-u}{s} \right)$$

Equation 3.2

represents a family of functions called wavelet basis functions, and * indicates a complex conjugate. The scale parameter can either compress or dilate the function. Equation 3.1 is called wavelet transform because the scale and time parameters u and s are assumed to be continual values (Kumar, 1997). Therefore, wavelet transform is a function of two variables (u, s). Both

$f(t)$ and $\psi(t)$ belong to $L^2(R)$, the set of square integrable functions (equation 3.1), also called the set of energy signals.

The translation gives time-related information. As the position of wavelets is shifted along the signal, wf gives the degree of correlation between the wavelet and the part of the signal around u.

$$A(u,s) = |wf(u,s)|$$

Equation 3.3

where $|wf(u,s)|$ is an amplitude spectrum. The phase is given by

$$\phi(u,s) = \arctan\left[\frac{\mathrm{Im}(wf(u,s))}{\mathrm{Re}(wf(u,s))}\right]$$

Equation 3.4

The power spectrum wavelet is defined as

$$Pf(u,s) = |wf(u,s)|^2$$

Equation 3.5

The power spectrum or energy density measures the time series variance at each scale and time.

3.3.4 Time-frequency localisation

The Fourier analysis uses Fourier (trigonometric) series to tells about frequencies present in the signal, although it is unable to distinguish between the signals**.** The Fourier transform offers valuable information about signals but it does not properly analyse signals whose frequency content changes in time. The method used to obtain the frequency content of a process as a function of time is called time-frequency analysis.

The advantage of wavelet transform is that it gives good time-frequency representation and has a changeable window function. Like a windowed Fourier transform, the wavelet transform technique can measure the time-frequency variations of spectral components, but it has a different time-frequency resolution (Mallat, 1998). The window function performs correlation and windowing at the same time. Wavelet transform is based on an octave band decomposition of the time-frequency plane, as shown in Fig. 3.5 (Kumar, 1997).

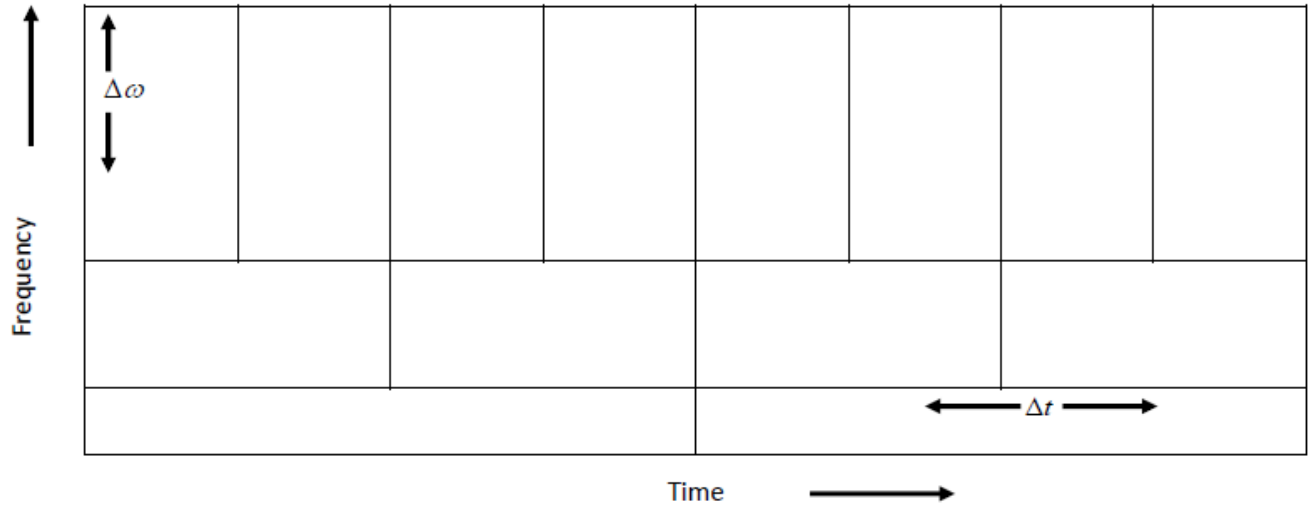

Figure 3.5. The vertical and horizontal dimensions of the frequency increase upward and time increase sideways**.**

Δt is the horizontal dimension of each cell while $\Delta\omega$ is the vertical dimension and the area is given by $\Delta t\Delta\omega$. For high frequencies, dimensions of the cells are shorter, which correspond to shorter window length. Therefore, the signal is better resolved in time and poorly resolved in frequency. In low frequencies, the horizontal dimensions are longer, which correspond to longer window length. As a result, the signal is better resolved in frequency and poorly resolved in time. Wavelet analysis is designed to give good time resolution and poor frequency resolution at high frequencies, and vice versa (Kumar, 1997; Mthembu, 2006).

3.4 The Fast Fourier transform

The FFT (fast Fourier transform) is an algorithm for computing the finite DFT (discrete Fourier transformer). The FFT is also the most vital algorithm and computer programme for doing spectrum analysis (McClellan, 1998). The FFT technique reduces the number of multiplications required from N^2 to a number proportional to $N \log N$ (Bracewell, 2000). This can lead to a decrease in execution time for large values of N. For a signal value of N points, we can directly calculate the N discrete Fourier sums by

$$\hat{f}(k) = \sum_{n=o}^{N-1} f(n) e^{-i\frac{2\pi kn}{N}}$$

Equation 3.6

where $0 \le k < N$ and N is the number of points for complex multiplications (complex products) and additions. The FFT algorithm reduces the numerical complexity to $N \log N$ by reorganizing the calculations.

Even frequency indices are given by

$$\hat{f}(2k) = \sum_{n=o}^{\frac{N}{2}-1} \left(f(n) + f\left(n + N/2\right) \right) e^{-i\frac{2\pi kn}{N/2}}$$

Equation 3.7

Odd frequency indices are also given by

$$\hat{f}(2k+1) = \sum_{n=o}^{N/2-1} \left(f(n) - f\left(n + N/2\right) \right) e^{-i\frac{2\pi kn}{N/2}}$$

Equation 3.8

The DFT of the $N/2$ periodic signal can be obtained by calculating the even frequencies,

$$f_e(n) = f(n) + f\left(n + N/2\right)$$

Equation 3.9

By computing the Fourier transform of the $N/2$ periodic signal, odd frequencies can be derived as

$$f_o(n) = e^{-i\frac{2\pi n}{N}}\left(f(n) - f\left(n + N/2\right)\right)$$

Equation 3.10

N is the size of the discrete Fourier transform which can be calculated with two discrete Fourier transforms of size $N/2$ plus 0 operators. The inverse Fourier transforms of f is the FFT and $f*$ is a complex conjugate given by,

$$f^*(k) = \frac{1}{N}\sum_{n=o}^{N-1} \hat{f}^*(k) e^{-i\frac{2\pi kn}{N}}$$

Equation 3.11

3.4.1 Cross spectrum density

Cross-correlation is the standard method of estimating the degree to which two series, $g(x)$ and $h(x)$, are correlated. The formula for the cross-correlation functions of $h(x)$ and $g(x)$ is

$$f(x) = g * f = \int_{-\infty}^{\infty} h(u) g(x-u) du$$

Equation 3.12

The signals $g(x)$ and $h(x)$ can be transformed to give $G(\omega)$ and $H(\omega)$. This can be expressed mathematically as,

$$CS = \frac{G_n * H_n}{\omega_0} = C_{gh}(\omega)\log\left(i\phi_{gh}(\omega)\right)$$

Equation 3.13

where C_{gh} is a cross spectrum amplitude at a specific frequency f while $\phi_{gh}(\omega)$ is the cross spectrum phase and G_n and H_n are the signals. This information can be used to calculate time lag for f between two signals. The lagging time is given by

$$\Delta t = \frac{\Delta\varphi}{2\pi \times f}$$

Equation 3.14

$\Delta\varphi$ is a phase shift in radians.

3.4.2 Frequency filtering

Frequency filtering is the multiplication of the Fourier transform with the filter function re-transformed into the spatial domain. In a frequency filtering process, attenuating high frequency results in smoother data in the spatial domain while attenuating low frequency enhance the edges. In addition, multiplying a Fourier transform with a filter in the Fourier space is identical to convolution in the spatial domain.

There are three types of frequency filtering processes: lowpass, highpass and bandpass filtering. A low pass filter attenuates high frequencies and leaves low frequencies unchanged. The results in the spatial domain are equivalent to that of smoothing filters, as it blocks high frequencies which correspond to sharp intensity changes (Smith, 1997). In addition, a low pass filter suppresses all frequencies higher than the cut-off frequency and leaves smaller frequencies unchanged.

A highpass filter yields edge enhancement or edge detection in the spatial domain because the edges contain many high frequencies. The advantage of bandpass filtering is that it attenuates

very low and high frequencies while keeping a middle range band of frequencies. It can be used to improve edges, suppressing low frequencies while reducing the noise at the same time (Bracewell, 2000).

In addition, bandpass filtering is done by applying the Fourier transform of the signal and multiplying it with a filter transfer function. It tends to have an inverse Fourier transform producing a filter signal of

$$A(u,v) = B(u,v)C(u,v)$$

Equation 3.15

where $C(u,v)$ is the Fourier transform and $B(u,v)$ is the filter transfer function. The Bandpass filter peaks respond within a narrow frequency range. The center frequency covers a range from $f_{\min}$ to $f_{\max}$.

Chapter 4 Gravity wave parameters

4.1 Introduction

The dynamics of the polar mesosphere and lower thermosphere are dominated by waves with periods ranging from a few minutes to months. These gravity waves (GWs), tides and planetary waves interact with the mean flow, determining the circulation and mean state of the atmosphere (Hibbins et al., 2005). GWs are filtered by the mean circulation in the stratosphere and mesosphere and accelerate the mean flow in the mesosphere, which leads to the lower thermospheric zonal wind reversal, meridional circulation and MLT temperatures (Jacobi et al., 2005).

Major wave influences occur between ~10 and 110 km altitudes in the middle atmosphere because of decreasing density and increasing wave amplitudes with altitude (Fritts and Alexander, 2003). Gravity waves control the wind/thermal balance in the MLT through wave dissipation and the accompanying momentum flux divergence (Fritts and Alexander, 2003; Pragati et al., 2010).

Gravity waves are important for understanding the energy and momentum flow in the MLT region (80–100 km above the earth) where they release momentum having propagated upwards from their respective generation regions in the troposphere and stratosphere (Pragati et al., 2010). Gravity waves are generated primarily within the troposphere by severe weather disturbances such as deep convection and strong orographic forcing (Fritts and Alexander, 2003; Jiang et al., 2004).

This chapter presents the wave extraction methodology, the characteristics of gravity wave parameters as well as the results seen in other instruments. The imaging riometer data for the year 2000 was used to extract wave parameters such as horizontal wavelengths, horizontal phase velocities, observed periods and horizontal propagation directions. The focal point of the study has been the seasonal behaviour of gravity wave parameters.

4.2 Wave extraction methodology

The SANAE imaging riometer (64 beams) was used in this study. The imaging riometers at SANAE (72˚S, 3˚W) and Halley (76˚S, 27˚W) in Antarctica are similar, both using the design outlined by Detrick and Rosenbank (1990). Each individual beam covers a different area because of the obliquity of its projection onto the horizontal layer as shown in Figure 3.2 (a).

The beams near the center are nearly circular while those near the corners form a distorted ellipse. Five center beams (20, 28, 36, 37 and 38) were selected as shown in Figure 4.1. According to Moffat-Griffin et al. (2008) it is easier to work with center beams because they give the full view and are not distorted as opposed to the beams that are further away (at the corners). The distances between the beams were computed using the method outlined by Wilson (2000) and were found to be 25 km between beams 20 & 28 and 37 & 38 and 22 km between beams 28 & 36 and 36 & 37. The separations between beams are graphically illustrated in Figure 4.1.

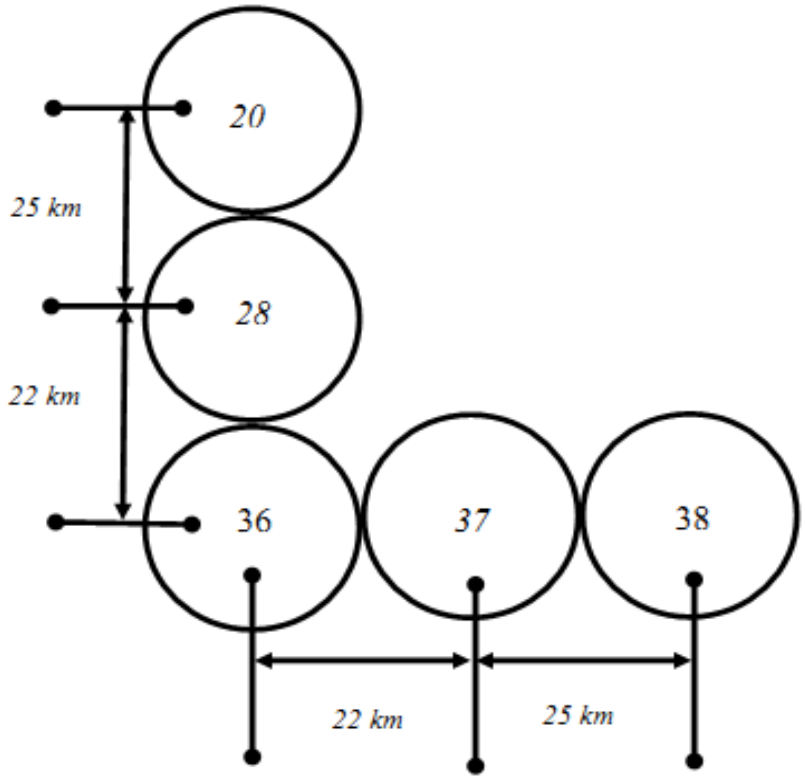

Figure 4.1. A **s**chematic representation of the selected beams, showing four beam distances.

It is possible to determine the gravity wave parameters by using two time-series to analyse the wave structure. The typical absorption time-series graphs are shown in Figure 4.2. This illustrates the imaging riometer data as measured by the beams, indicating similar wave peaks (peak events) of between 800 and 1000 minutes. Absorption (amplitude) is different for every beam, i.e. the strength or power varies in each beam.

The wavelet analysis technique was employed to analyse the absorption data. This method is used in scientific fields to study non-stationary time-series as well as the frequency-varying or time-varying events that have non-stationary phases throughout the time-series such as gravity waves, tides and planetary waves (Grinsted et al., 2004; Maraun and Kurths, 2004). This analysis technique gives information on the time duration of the given event and the frequency content.

In this study, the complex wavelet was utilised as the mother wavelet and the procedure used to extract wave parameters, periods and wave durations of the events was applied to the spectrum components.

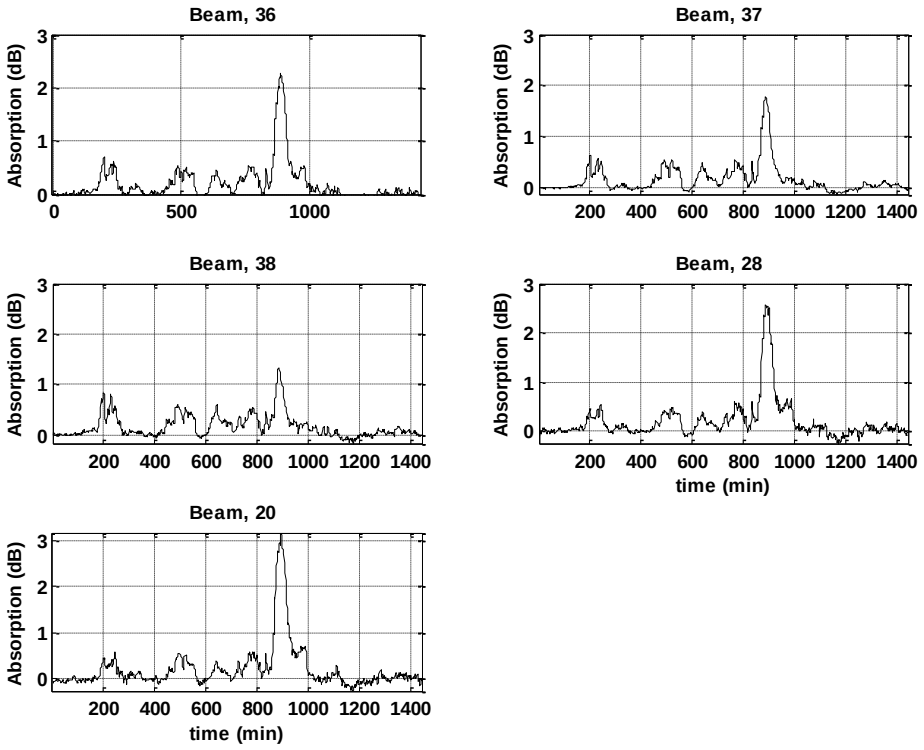

Figure 4.2. Typical absorption time series plots using imaging riometer data for 14 February 2000.

The method outlined by Moffat-Griffin et al. (2008) was used to extract wave parameters from the imaging riometer data. In this chapter, phase difference was obtained by using the FFT (Fast Fourier Transform). Using the data from the two adjacent beams, the phase difference between spectral components was computed using the CSD (cross spectral density), which is defined as the Fourier transform of the cross correlation between two time-series data (see chapter 3).

Based on the knowledge of the distance between the adjacent beams, the phase difference between the spectral components and the period of the wave feature, the horizontal phase speed and horizontal wavelength is calculated using equations 4.1 and 4.2, respectively:

$$\lambda_p = \frac{2\pi\Delta x}{\Delta\phi}$$

Equation 4.1

$$V_p = \frac{\lambda_p}{T}$$

Equation 4.2

where change in x (Δx) measured in km is the distance between beams, $\Delta\phi$ is the phase difference between the beams in radians and T is the period in seconds.

The spatial resolution of the SANAE IRIS (imaging riometer for ionospheric studies) puts a limitation on the resolvable horizontal wavelength to $2\Delta x$. Any waves that pass through the field of view with a horizontal wavelength of less than $2\Delta x$ would be subject to spatial aliasing, resulting in the parameters obtained being unreliable (Moffat-Griffin et al., 2008). Eradicating this spatial aliasing requires a wave feature to be detected in the three linearly adjacent beams over the same time range. Using simple wave theory, a spatial aliasing method can be derived as

$$\frac{d_{36,37}}{d_{37,38}} = \frac{\Delta\phi_{36,37}}{\Delta\phi_{37,38}}$$

or

$$\frac{d_{36,28}}{d_{28,20}} = \frac{\Delta\phi_{36,28}}{\Delta\phi_{28,20}}$$

Equation 4.3

where $d_{36,37}$, $d_{36,28}$, $d_{37,38}$, and $d_{28,20}$ are the beam separations while $\Delta\phi_{36,37}$, $\Delta\phi_{36,28}$, $\Delta\phi_{37,38}$, and $\Delta\phi_{28,20}$ are phase differences. Therefore, using the right hand side of equation 4.3, the phase difference can be adjusted by a factor $\pm 2n\pi$ (n is an integer) until the best match to the beams

is found. The adjusted phase difference is thereafter used in equations 4.1 and 4.2 to calculate the true wave parameters.

Ultimately, the method outlined by Donelan et al. (1990) in their application of the method to ocean waves, was used to calculate the direction of the wave. The wave propagation direction is given by,

$$\theta = \arctan\left(\frac{\Delta\phi_{36,28}}{\Delta\phi_{36,37}}\right)$$

Equation 4.4

The phase difference between imaging riometer beams north-south and east-west is at 90˚. The subscripts 36,28 and 36,37 refer to the north-south and east-west beams, respectively. In this case, 0˚ and 360˚ are pointing north, with the angle increasing in a clockwise direction.

4.3 Wave parameter extraction

The analysis started with the computation of the wavelet transform, using data from all five beams mentioned above to identify the dominant spectral components. Gravity wave parameters were computed where there was a common spectral component in all beams, which can sometimes show different absorption (amplitude) as long as they happen in the same period. The wavelet transform has the capability of identifying spectral components and their time of occurrence.

Figure 4.3 shows the ionospheric absorption measured during the same wave event in the five most central beams aligned along the north-south to east-west direction of the imaging riometer. The spectra show the dominant spectral component observed at 15.5 hours on 14 February 2000 (day number 45 of the year 2000) as seen in Figure 4.3.

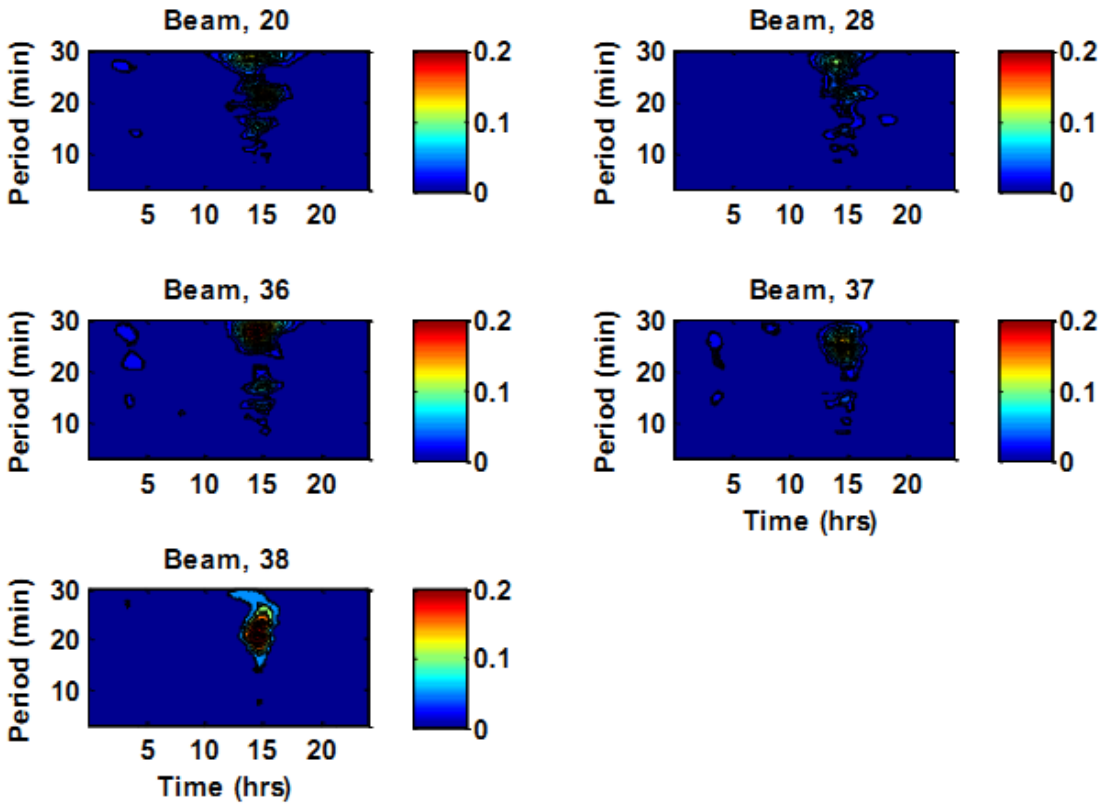

Figure 4.3. Contour wavelet plots of beams 20, 28, 36, 37 and 38 for day 45 of the year 2000.

This is one of the spectral components that were extracted. The wavelet method was used to identify the period of interest and calculate the wave parameters using the FFT technique. Using equations 4.1-4.4, the gravity waves parameters such as the horizontal phase speeds, horizontal wavelengths and horizontal propagation directions were calculated. The results were extracted and are shown in Table 4.1, the focus being on the short period gravity waves in the periods ranging from 5-60 min.

Table 4.1**.** A selection of results of gravity wave parameters at SANAE.

Day	T (min)	Velocity ($m.s^{-1}$)	Wavelength (km)	Direction (deg)	Adjust
45	20	26	32	317	y
84	15	37	32	226	y
93	53	19	60	40	y
96	21	25	32	314	y
100	26	21	32	47	y
105	42	27	69	47	y
119	21	26	32	319	y
122	13	40	32	134	y
126	15	35	33	317	y
154	16	33	32	135	y
156	21	26	33	48	y
158	58	29	100	74	y
188	18	33	36	128	y
214	23	24	33	45	y
240	27	21	34	56	y
244	10	51	31	314	y

4.4 Gravity waves characteristics

The procedure described in section 4.3 was applied in these results. Gravity wave parameters versus Day numbers were plotted to investigate the behaviour of the day-to-day variation of gravity wave characteristics. Gravity wave parameters were extracted for the months of April, June, September and December representing (a) autumn, (b) winter, (c) spring and (d) summer, respectively.

Figures 4.4 and 4.5 show the seasonal behaviour of gravity wave parameters at SANAE. Fig. 4.4 shows four seasonal variations of the horizontal wavelengths ranging from 10 to 100 km. There is no clear seasonal variation that could be deduced from these figures. They show almost the same average on the horizontal wavelength for spring and autumn, i.e. ~58 and ~62 km for spring and autumn (see Figs. 4.4 (a) & (c)), respectively. The average horizontal wavelengths are similar for summer and winter (~65 km) (see Figs. 4.4 (d) & (b)).

A similar study was done by Bageston et al. (2009). These authors investigated the mesospheric gravity waves at Comandante Ferraz Antarctica station (62˚S, 58.4˚W) between April and October 2007. They found the horizontal wavelengths to be from 10-60 km with phase speeds of 5-115 $m.s^{-1}$. The horizontal propagation direction was towards the south-west in winter while during spring it was propagating towards the north-west. Their study was done using an airglow all sky imager. The horizontal wavelengths results found in this study range from ~10–100 km, which are not very different from the results of Bageston et al. (2009).

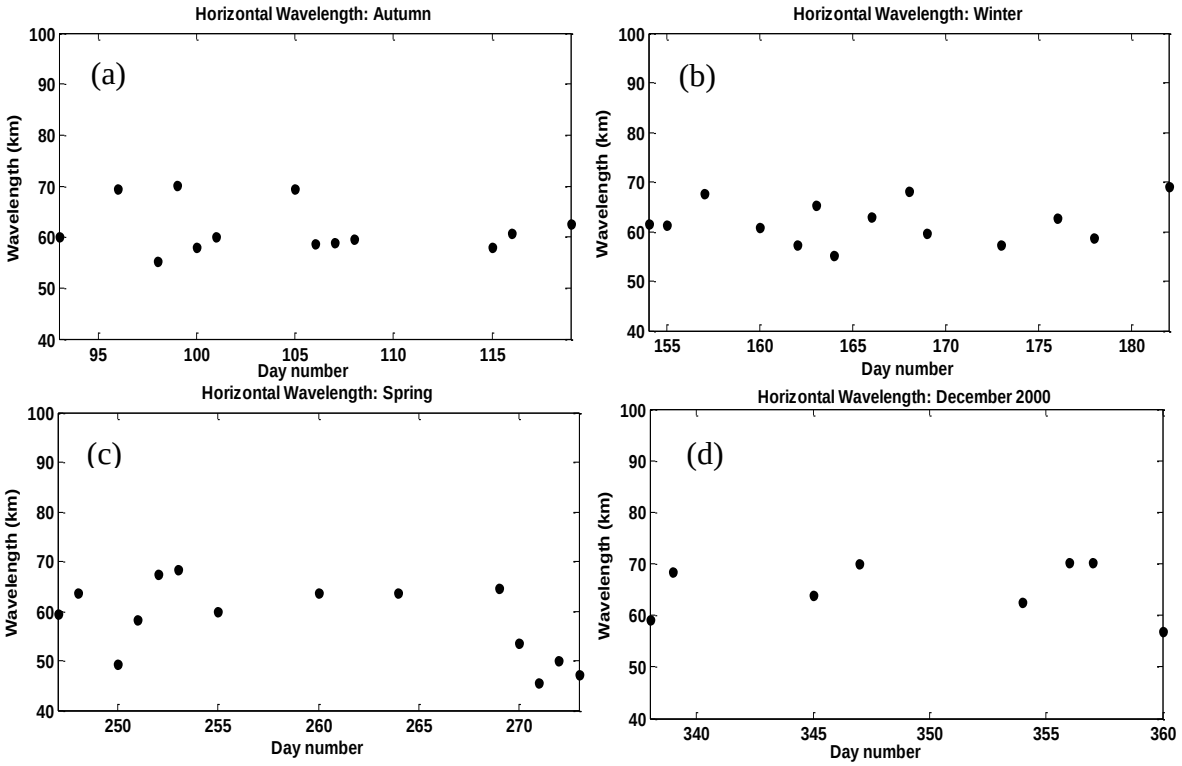

Figure 4.4. The seasonal variation of the horizontal wavelengths for (a) autumn, (b) winter, (c) spring and (d) summer in 2000.

Fig. 4.5 shows the seasonal variations of the horizontal phase velocities, ranging from 10 to 60 $m.s^{-1}$. Spring and autumn have identical average horizontal phase velocities while winter has higher average horizontal phase velocities than summer. The average horizontal phase velocity is ~23 $m.s^{-1}$ for spring and autumn (see Figs. 4.5 (d) & (b)) and ~22 $m.s^{-1}$ and ~27 $m.s^{-1}$ for summer and winter (see Figs. 4.5 (c) & (a)), respectively. The seasonal variations of the horizontal phase velocities are typically the same for each season.

At Allahabad (25.4˚N, 81.8˚E) Pragati et al. (2010) studied the characteristics of gravity waves in the upper mesosphere region, using OH airglow imaging. These authors noticed the day-to-day variation of wave parameters in all the seasons, particularly in the horizontal phase velocities and horizontal wavelengths. Their results range from 10-48 $m.s^{-1}$ and 10-37 km for the horizontal phase velocities and horizontal wavelengths, respectively. The horizontal propagation directions are north and north-eastward in April and May. In February and March, the directions are south-

westward. In the imaging riometer results of this study, the horizontal phase velocities range from 17-60 $m.s^{-1}$, which are comparable to results presented by Pragati et al. (2010). The only difference is that this study was done at high latitude while their study was done at low latitude.

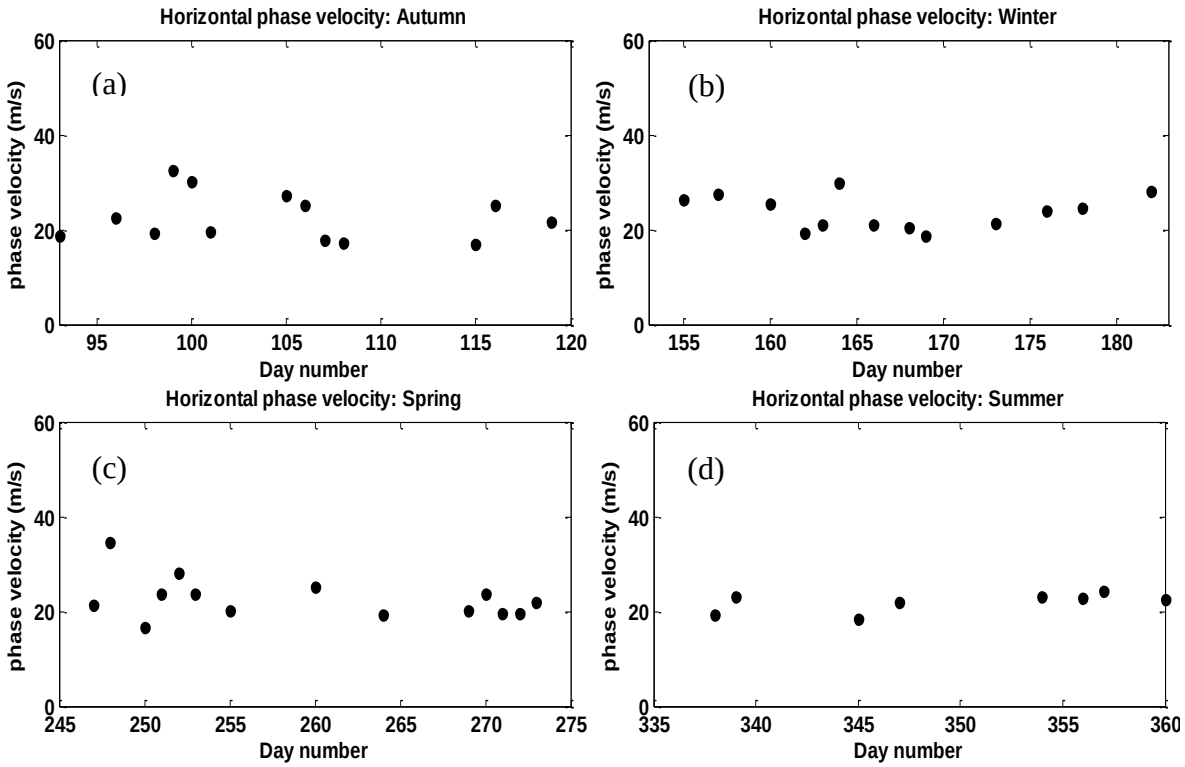

Figure 4.5. The seasonal variation of the horizontal phase velocities for (a) autumn, (b) winter, (c) spring and (d) summer in 2000.

The objective of this study is to investigate the seasonal variations of the horizontal propagation direction by studying the different seasons. Fig. 4.6 shows the day versus horizontal propagation direction in degrees. The months selected are the same as in Figs. 4.4 and 4.5. The typical horizontal propagation directions range from 40-50˚, 30-80˚, 40-60˚ and 35-60˚ for autumn (a), winter (b), spring (c) and summer (d), respectively. The horizontal propagation directions of all four seasons appear to be north-eastward as can be seen especially for June (see Fig. 4.6 (b)). The average horizontal propagation direction is 48˚. One of the factors contributing to this may be high gravity wave activity in winter.

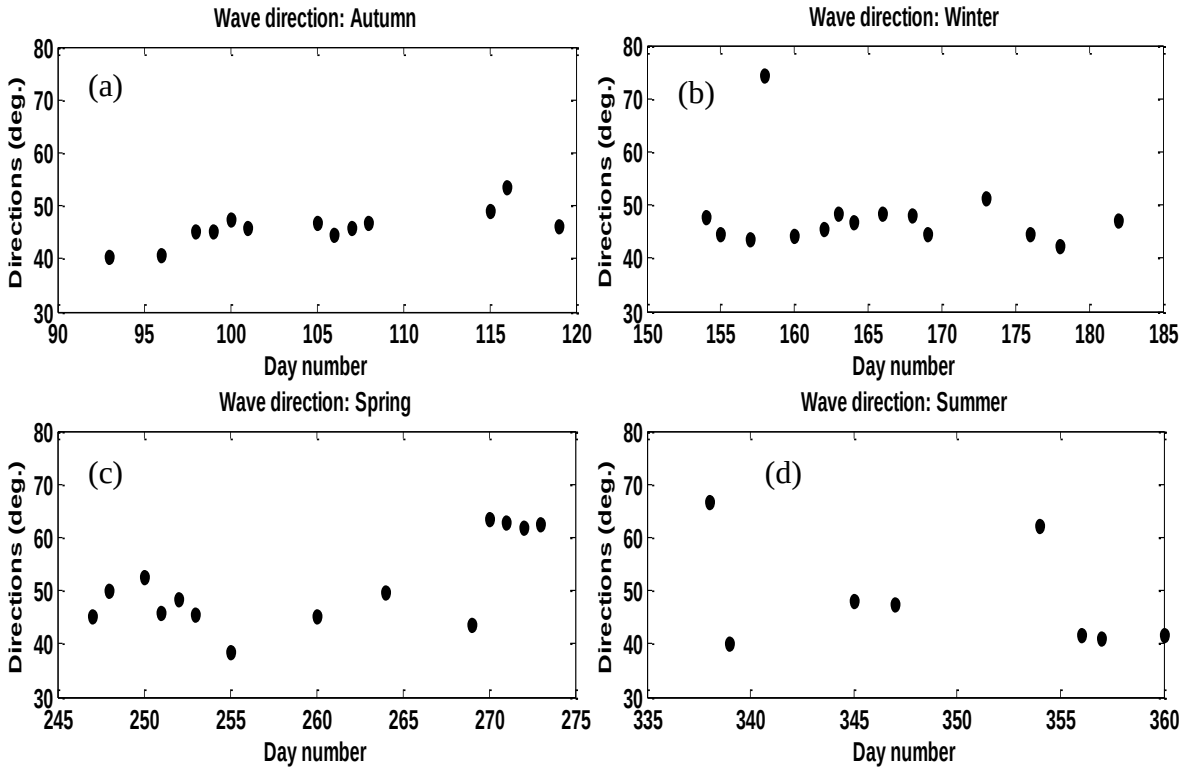

Figure 4.6. The seasonal variation behaviour of the horizontal propagation direction for (a) autumn, (b) winter, (c) spring and (d) summer in 2000.

A further study was done to investigate the relationship between the horizontal propagation directions and horizontal wavelengths. The aim was to observe the seasonal behaviour of these two parameters. The method used to calculate the relationship between these two parameters was the linear least squares fitting, polynomial fit, which returns the coefficients of the best fit polynomial and polynomial values. The degree of the fitting polynomial is $n = 1$ (a straight line).

Fig. 4.7 shows the horizontal propagation directions distributed from 30˚ to 80˚ and the horizontal wavelengths from 40 to 120 km. In these figures, R^2 shows poor correlation (see Figs. 4.7 (a), (b) & (d)), except for Fig. 4.7 (c), which shows good correlation. Most slopes are meaningless because R^2 are smaller (see Figs. 4.7 (a), (b) & (d)). However, Fig. 4.7 (c) shows good correlation with the slope of -0.71 ($R^2 = 58\%$). This shows the increase in the horizontal propagation directions increase the horizontal wavelengths (see Fig. 4.7 (c)). These results depend on the seasonal variations in the background wind field (Stockwell and Lowe, 2001).

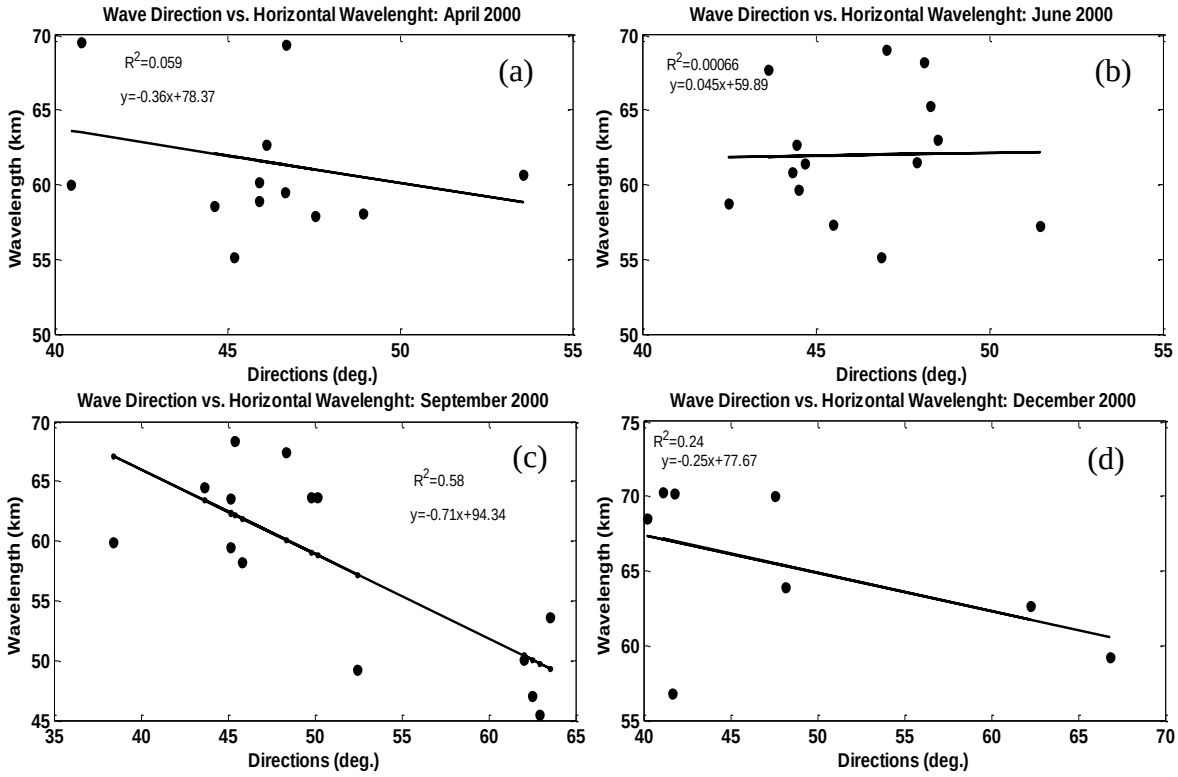

Figure 4.7. Wave direction plots showing horizontal wavelength distributions of short gravity waves for (a) April, (b) June, (c) September and (d) December in 2000. Solid line indicates the best fit line.

The same method as used in Fig. 4.7 was applied to investigate the relationship between the horizontal propagation directions and horizontal phase velocities (see Fig. 4.8). Horizontal propagation directions are distributed from 30˚ to 60˚, while the horizontal phase velocities spread from 15 to 40 m.s^{-1}. In this figure, there is no convincing relationship that can be concluded between the horizontal propagation directions and phase velocities. All the figures show poor correlation with slopes of 0.23 ($R^2 = 21\%$), 0.12 ($R^2 = 0.76\%$), -0.071 ($R^2 = 1.7\%$) and -0.090 ($R^2 = 21\%$) for April, June, September and December, respectively. These results show that the wave parameters depend on seasonal variability.

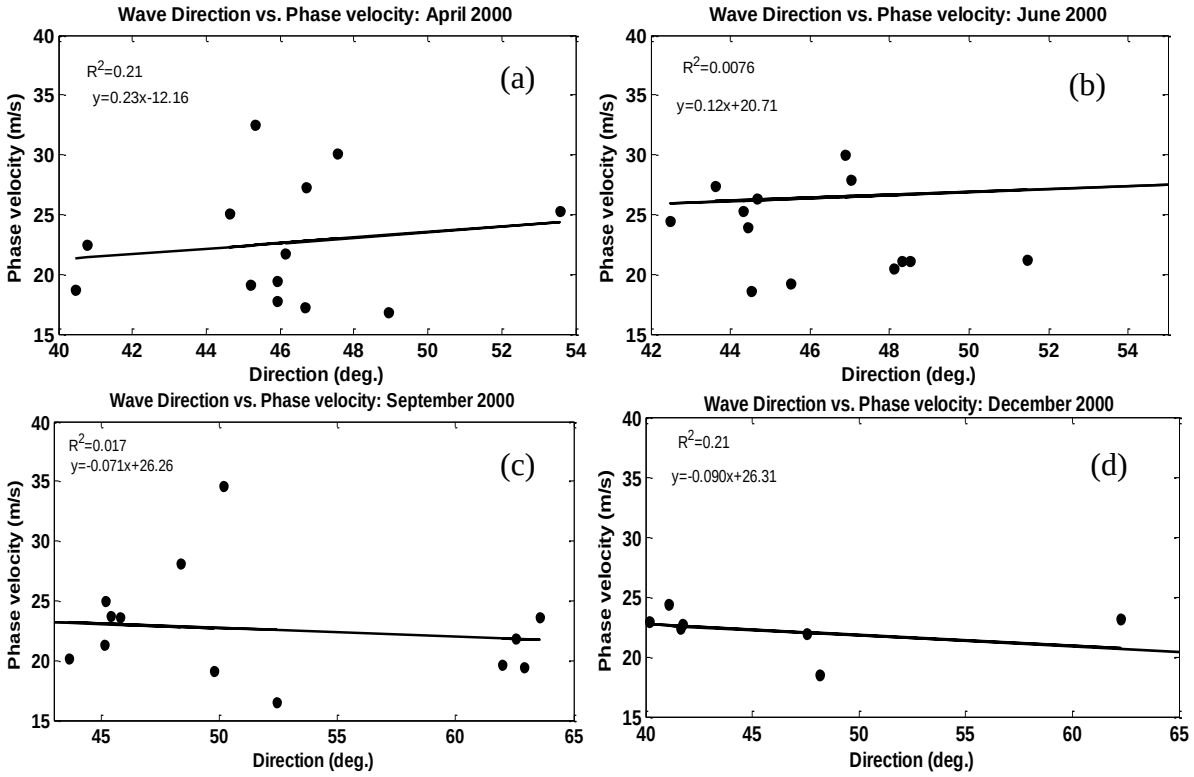

Figure 4.8. Wave direction plots showing horizontal phase velocity distributions of short gravity waves for (a) April, (b) June, (c) September and (d) December in 2000. Solid line indicates the best fit line.

This study was motivated by the findings of Nielsen et al. (2009). These authors studied the relationship between horizontal wavelengths, phase speeds and horizontal propagation direction. Their results show the variation of the horizontal wavelengths (phase speeds), with small wavelengths (phase speeds) dominating the westward, and longer wavelengths (higher phase speeds) characterising the eastward motion. They used an all sky airglow imager to study the climatology of a short period mesospheric gravity wave over Halley in Antarctica. The authors explained the trends they observed as consistent with the critical layer filtering of the waves by seasonal variations in the background wind. Other authors who have done similar studies in different hemispheres (Bageston et al., 2010; Taylor et al., 2009; Pragati et al., 2010) have focused on the extraction of the short period of gravity wave parameters.

To further investigate the relationship between gravity wave parameters and wind components, UKMO zonal mean wind data were analysed at 70˚S in order to determine whether the zonal mean wind has an effect on wave parameters. This process is called critical layer filtering. Filtering occurs when the background wind field in the direction of wave motion matches the observed phase speeds, and the waves are absorbed into the background mean flow (Hines and Reddy, 1967; Nielsen et al., 2009).

In this study, the wind information from the UKMO model was used to study potential effects of critical filtering over SANAE. If the background wind and horizontal phase velocities are moving in the same direction as the background wind, critical filtering may occur. However, if the background wind and horizontal phase velocities are moving in opposite directions, no critical filtering will take place irrespective of their wind magnitude components. This will be the approach used to determine whether filtering occurs or not.

Fig. 4.9 shows the zonal mean wind for four months in 2000 (April, June, September and December), representing autumn, winter, spring and summer, respectively. Zonal mean winds are very low at altitude of 20-100 hPa but as altitude increases from 20-1 hPa, the zonal mean winds become higher (Fig. 4.9). Spring (Fig. 4.9 (c)) and winter (Fig. 4.9 (b)) have very high zonal mean winds while the wind speeds are weaker for autumn (Fig. 4.9 (a)) and summer (Fig. 4.9 (d)). The zonal mean winds can reach up to ~60 $m.s^{-1}$, particularly in spring, whereas the minimum wind speeds are ~20 $m.s^{-1}$ for both summer and autumn. The zonal average wind directions are eastward in all seasons. The strongest zonal mean winds are seen at high altitudes (~60 km) in all seasons except in summer (December) where the zonal mean winds are very weak.

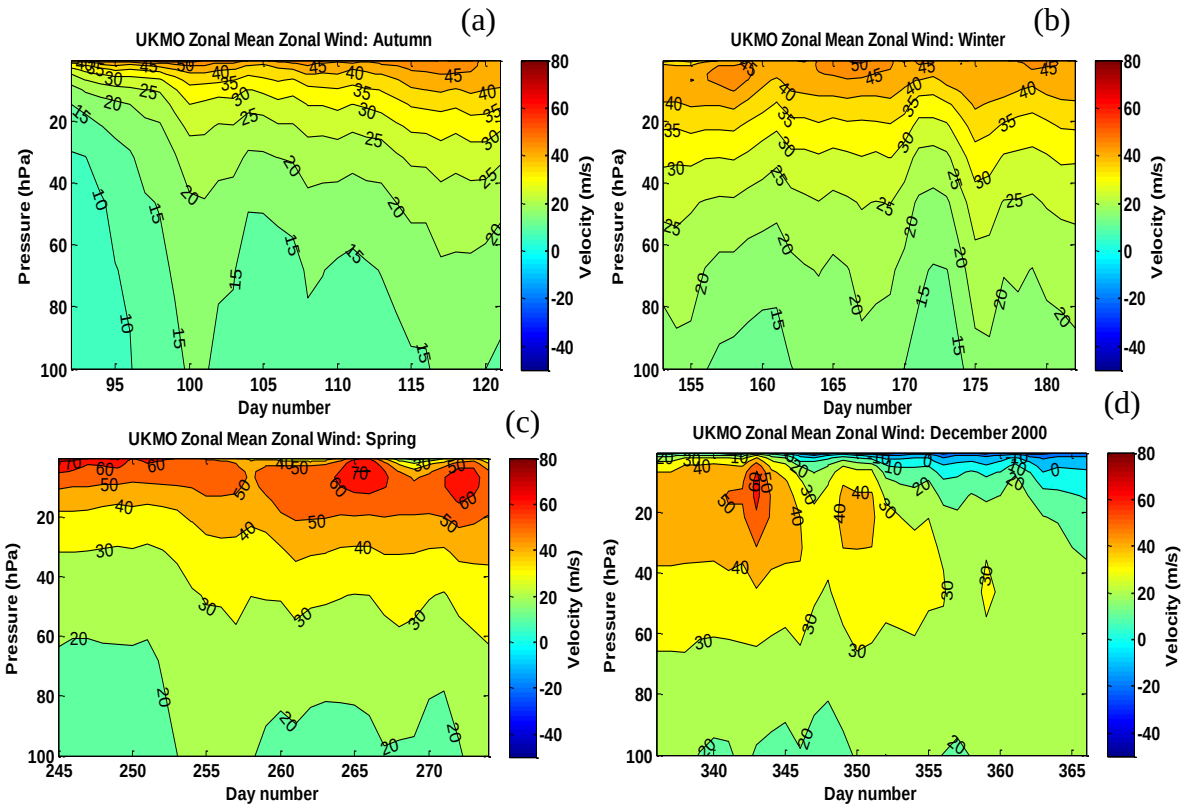

Figure 4.9. UKMO zonal mean zonal winds for (a) autumn, (b) winter, (c) spring, and (d) summer for the year 2000, obtained using the UKMO model.

Therefore, waves with horizontal phase speeds comparable to the background wind moving in the same direction as of the the waves, will be filtered. However, waves with phase speeds less or greater than background wind moving in the same direction as the waves, will not be filtered. As a result, waves propagating upward from the lower atmosphere are absorbed into the mean flow as they approach a critical layer and the intrinsic frequency of the waves are Doppler shifted to zero.

Smaller wave activity is therefore attributed to waves with small phase velocities experiencing a critical level of filtering. Where wave activity is larger, less filtering occurs and strong background wind is likely to cause a Doppler shift of waves to longer vertical wavelengths, which can reach larger amplitudes before saturating (Baumgaertner and McDonald, 2007). The situation occurs at any height when the local horizontal wind speed along the direction of propagation equals the observed horizontal phase speed of the gravity wave (Bageston et al.,

2009). In this case, some of the extracted wave parameters will be filtered whereas some will manage to propagate upwards into the upper atmosphere without being filtered and may be found in the mesosphere region.

In order to understand the filtering effects at a mesospheric height, HF radar wind data (zonal wind component) were used to observe the wind direction and velocities (amplitudes) for the selected seasons at ~90 km. The results from imaging riometer extracted wave parameters and HF radar data were compared. The observations for most of the months in the HF radar show a zonal wind of less than ±20 $m.s^{-1}$. The wave direction is eastward for April (a), June (b) and September (c), whereas it propagates westward for December (d).

Fig. 4.10 shows the seasonal behaviour at the SANAE HF radar for all the seasons. Although the mesospheric wind amplitudes are expected to be of notably larger amplitude, the high horizontal phase velocities of the waves (average ~24 $m.s^{-1}$) imply that mesospheric wind variability was most likely not the source of the observed anisotropy.

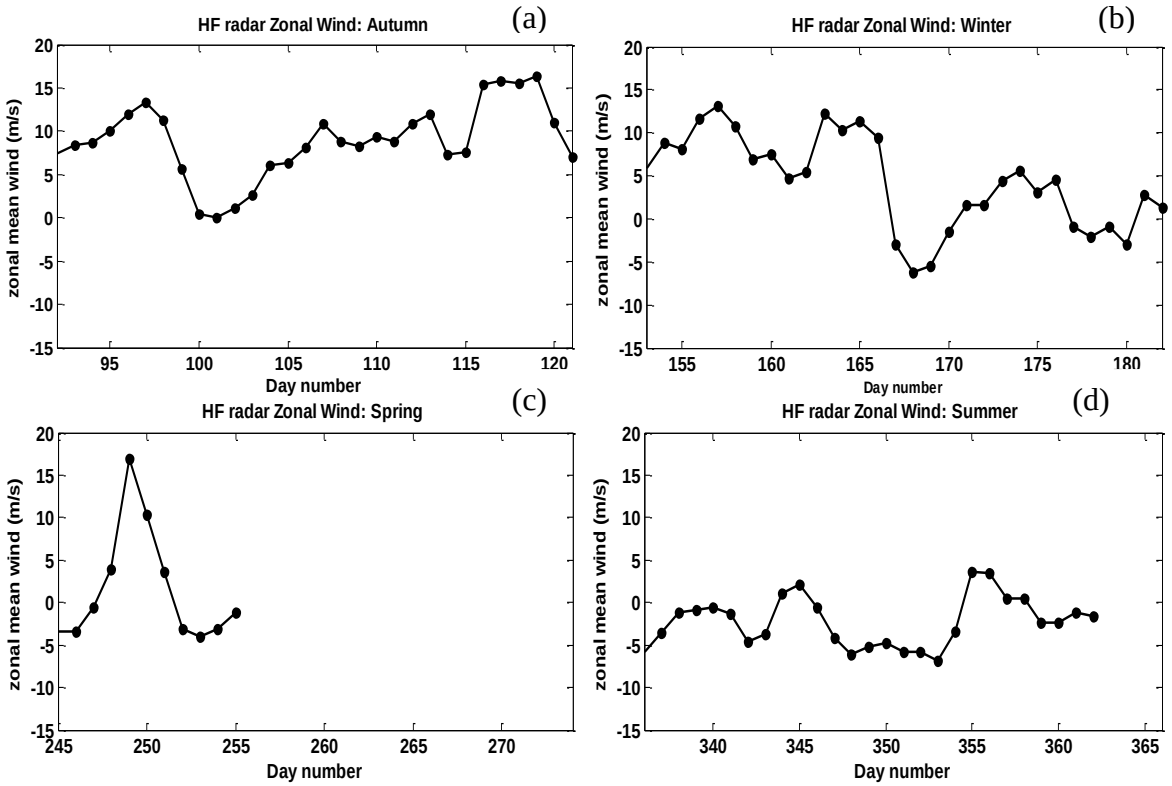

Figure 4.10. SANAE zonal mean wind for (a) autumn, (b) winter, (c) spring, and (d) summer for the year 2000, obtained using the HF radar.

4.5 Summary

An imaging riometer was used to extract wave parameters (observed periods, horizontal wavelengths, horizontal velocities and horizontal propagation directions) of the short period mesospheric gravity waves over SANAE, Antarctica (72˚S, 3˚W). This chapter provides the seasonal investigation of these waves at high latitude. Data analysis was performed over four months (April, June, September and December) of the year 2000. The main gravity wave characteristics were the horizontal wavelengths (~10-100 km), observed periods (~3-60 minutes), horizontal phase velocities (~5-60 $m.s^{-1}$), and horizontal propagation directions (~10-80˚). The horizontal propagation directions of the waves show a distribution with most of them propagating northeastward with an average of ~50˚.

The wave propagation direction in the mesosphere region depends on two factors, the source location in the lower atmosphere and the background wind field in the stratosphere and

mesosphere. This chapter focuses on the use of UKMO model data to determine seasonal variations and to investigate potential wind effects on critical filtering over SANAE. Critical filtering occurs when the background wind field in the horizontal propagation direction matches the horizontal phase velocity and the wave is absorbed into the background wind flow.

The horizontal propagation directions are mostly eastward from 100-0.3 hPa for the UKMO model data. The most dominant zonal winds are found at the upper stratosphere (0.316 hPa or ~60 km) and range from ~30-60 $m.s^{-1}$. The observed horizontal phase velocities are less than 45 $m.s^{-1}$ for all seasons, and the horizontal propagation direction is mainly northeastward as mentioned above. This suggests that the observed systematic variation in the magnitude of the wave parameters and their direction of propagating is most probably not only due to wind filtering effects, but also to a contribution from other sources e.g. baroclinic weather systems (storms and earthquakes), etc. (Bageston et al., 2009).

Chapter 5 Mean winds and planetary waves

5.1 Introduction

The circulation of the middle atmosphere is governed by the momentum deposition from various atmospheric motions, including propagating atmospheric waves such as planetary waves, gravity waves and tides. The atmospheric wave interaction with the mean flow causes processes such as wave breaking, filtering, mean wind reversal and MLT (mesosphere and lower thermosphere) heating and cooling (Fritts et al., 1999; Dowdy et al., 2005). This chapter discusses mean winds and planetary waves and focuses especially on the dynamics of the middle atmosphere. The planetary waves of interest are those with periods of between 2 and 20 days. This is mainly because the MLT region is known to have a strong presence of waves with recurring periods of 2, 5, 10, 14 and 16 days.

The planetary scale waves that are usually observed in the MLT region are known to be of tropospheric origin. They are generated by topographic and thermal features and propagate upwards. The instabilities arising from the horizontal and vertical gradients in the temperature and wind disturbances can also induce planetary waves. These waves are known to propagate both horizontally and vertically, carrying momentum into the middle and upper layers of the atmosphere (Fritts et al., 1999).

In this chapter, the meridional and zonal wind components are measured using SuperDARN HF (high frequency) radars. The results are used to study the dynamics of the MLT in terms of planetary wave activity. The SuperDARN HF radar wind data were measured at the two Southern Hemisphere high latitude stations, namely, Halley (76˚S, 27˚W) and SANAE (72˚S, 3˚W). The characteristics of the planetary wave, the quasi 2-day wave, the relationship between quasi 2-day wave power and the mean flow, as well as zonal wavenumbers are presented in this chapter.

5.2 Spectral characteristics

Both the wavelet analysis and STFT (short term Fourier transforms) spectral analysis techniques were applied to the SuperDARN HF radar wind data to investigate the planetary wave activity in the MLT region. The data used in this chapter were measured for the years 2000 to 2002. The STFT method was used to perform dynamic Fourier spectra, using a 28-day data window that was shifted forward by 1 day at a time.

The deduced power for a given data window was attributed to a central day as given by day 14 of a particular 28-day data interval. A long data window such as this usually results in the desired frequency resolution of 0.0357 cpd (cycles per day). However, the problem with this frequency resolution is that it is at the expense of time resolution. This is mainly important in this research, because planetary waves with short periods such as quasi 2-day waves, are characterised by bursts of wave activity that vary on scales of several days (Pancheva et al., 2008; Malinga and Ruohoniemi, 2007).

Figure 5.1 represents the evolution of hourly averaged zonal (a) and meridional (b) winds as observed by the SANAE HF radar during February 2002. For the purpose of this chapter, the daily mean wind was deduced by averaging the 4-day time sequence of the hourly averaged horizontal wind velocities measured by the SANAE and Halley HF radars at ~90 km altitude. The average mean wind measured by these radars is approximately ±8 $m.s^{-1}$ and ±3.5 $m.s^{-1}$ for the zonal and meridional components, respectively, depending on the season.

The 4-day data window was advanced by 1 day at a time, and the average of the data window was attributed to the second day of the interval. There were some periods where the instruments did not take measurements due to problems with the system. A 4-day mean was considered to be acceptable if at least 60% of the possible hourly wind values were recorded.

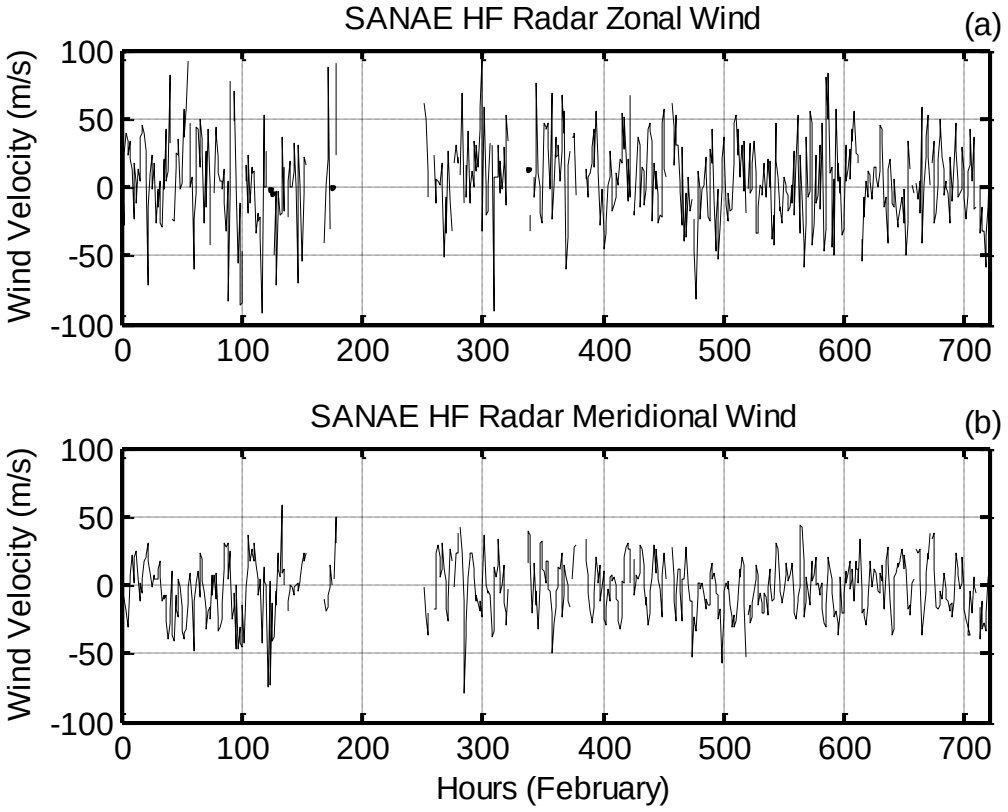

Figure 5.1. Hourly averaged zonal (a) and meridional (b) winds as observed by the SANAE HF radar during February 2002.

Fig. 5.2 shows a one-to-one comparison of the zonal (left column) and meridional (right column) mean flow of the hourly wind measured at SANAE (black solid line) and Halley (blue dotted line) for the years 2000 to 2002. The observations indicate good agreement between the two stations for both the zonal and meridional mean flow, with the zonal wind component being consistently stronger than the meridional wind. This is similar to results noted by other authors (Malinga and Poole, 2004; Jacobi et al., 1996). A strong MLT zonal mean flow reversal, which is associated with the unprecedented stratospheric warming in late winter of the year 2002, was also clearly detected by both HF radars.

Generally, the zonal mean flow shows stronger seasonal variability (with changes of up to a maximum of about 22 $m.s^{-1}$) than the meridional mean flow. At both sites, the zonal mean wind

is dominated by an eastward (positive) mean flow. However, there are instances where it also turns in the westward direction (especially during the summer and winter seasons). At both stations the observations indicate that the meridional mean flow is southward (negative) and northward (positive) as seen in Fig. 5.2.

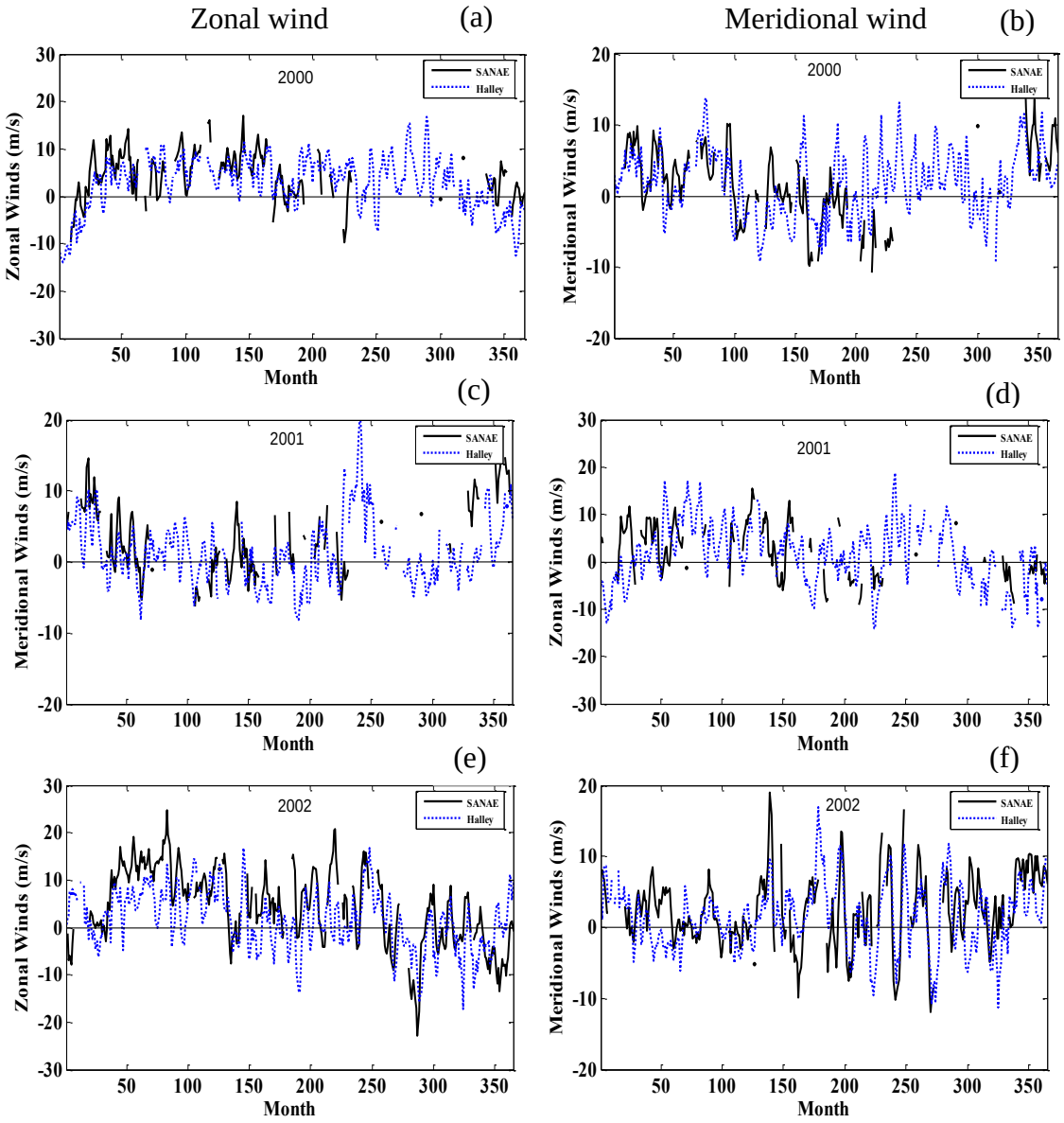

Figure 5.2. The zonal and meridional winds at SANAE (solid black line) and Halley (blue dotted line) stations in the southern hemisphere for the years 2000-2001.

Fig. 5.3 represents the zonal (left column, a, c, e) and meridional mean winds (right column, b, d, f). Most of these waves are observed in early winter and can be seen on day number ~100. They are mostly quasi 10- and 14-day waves with a maximum wave power of ~100 $m^2.s^{-2}$ and 300 $m^2.s^{-2}$ for both zonal and meridional mean winds, respectively. Also, the 10- and 14-day waves were detected in summer for zonal and meridional wind components (see Figs. 5.3 (a), (c) & (d)). A wave period of ~11 days with wave activity lasting ~2 days was observed on day number ~300 for zonal mean winds (see Fig. 5.3 (e)).

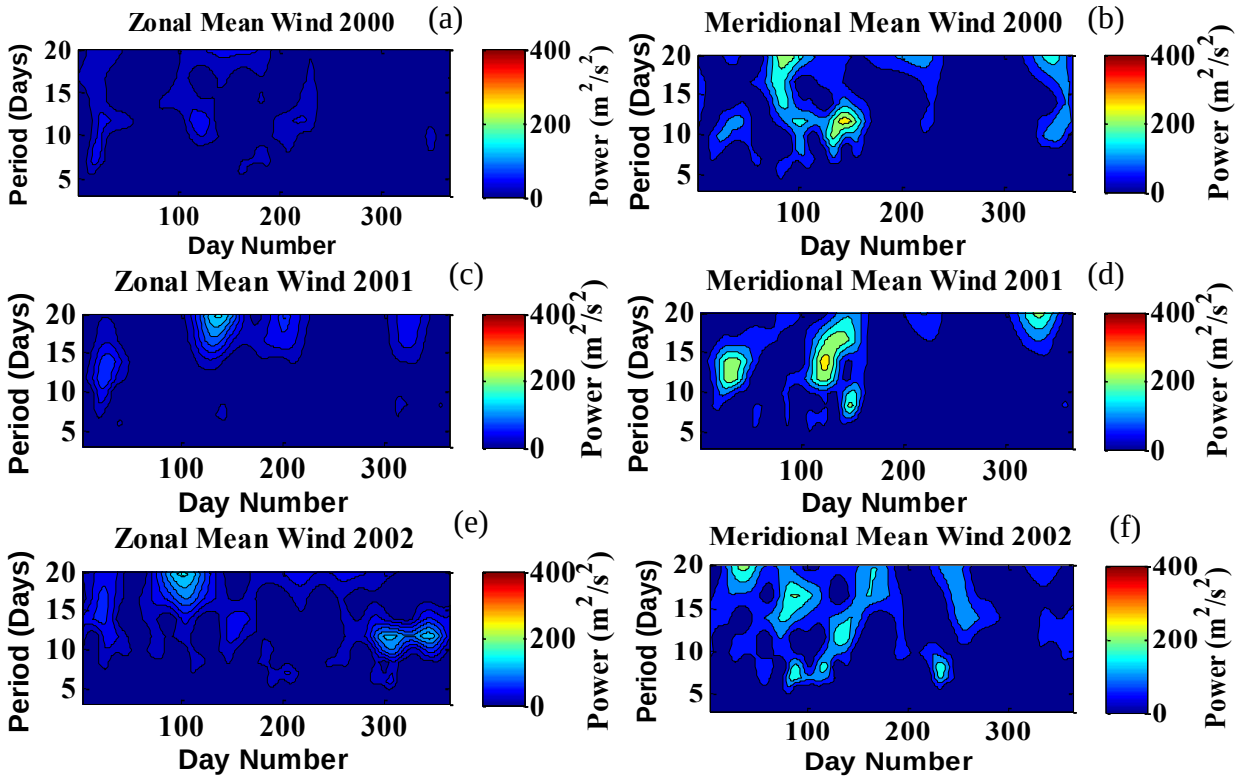

Figure 5.3. Wavelet spectra of zonal (left column, a, c, e) and meridional (right column, b, d, f) mean winds from SuperDARN HF radar at SANAE (72˚S, 3˚W) during 2000, 2001 and 2002 at ~90 km.

A similar study to the one at SANAE station was conducted for Halley. Fig. 5.4 shows the wavelet analysis for 2000-2002 of the seasonal evolution of the zonal and meridional mean winds. These plots reveal distinct planetary wave activity over Halley where wave periods from 3 to 20 days were observed with a wave activity lasting ~2-5 days. Wave activity is strong

around summer and winter at Halley. This shows that there is considerable interannual variability in the wave activity of the different wave components.

Strong wave activity was observed in the zonal (Fig. 5.4, left column) and meridional (Fig. 5.4, right column) mean winds on day number ~200. The wave power is about 200 $m^2.s^{-2}$ and 400 $m^2.s^{-2}$ for zonal and meridional mean winds, respectively. Most of these waves occur in the winter months and their wave activity lasted over 2 days. Quasi 10-day waves were observed in the meridional mean wind on day number 100 during the years 2000-2002 (Fig. 5.4, left column). These 10-day waves have wave power of less than 200 $m^2.s^{-2}$ and a wave activity lasting less than 2 days. At Halley station, the meridional wave power is stronger than the zonal wave power (see Fig. 5.4).

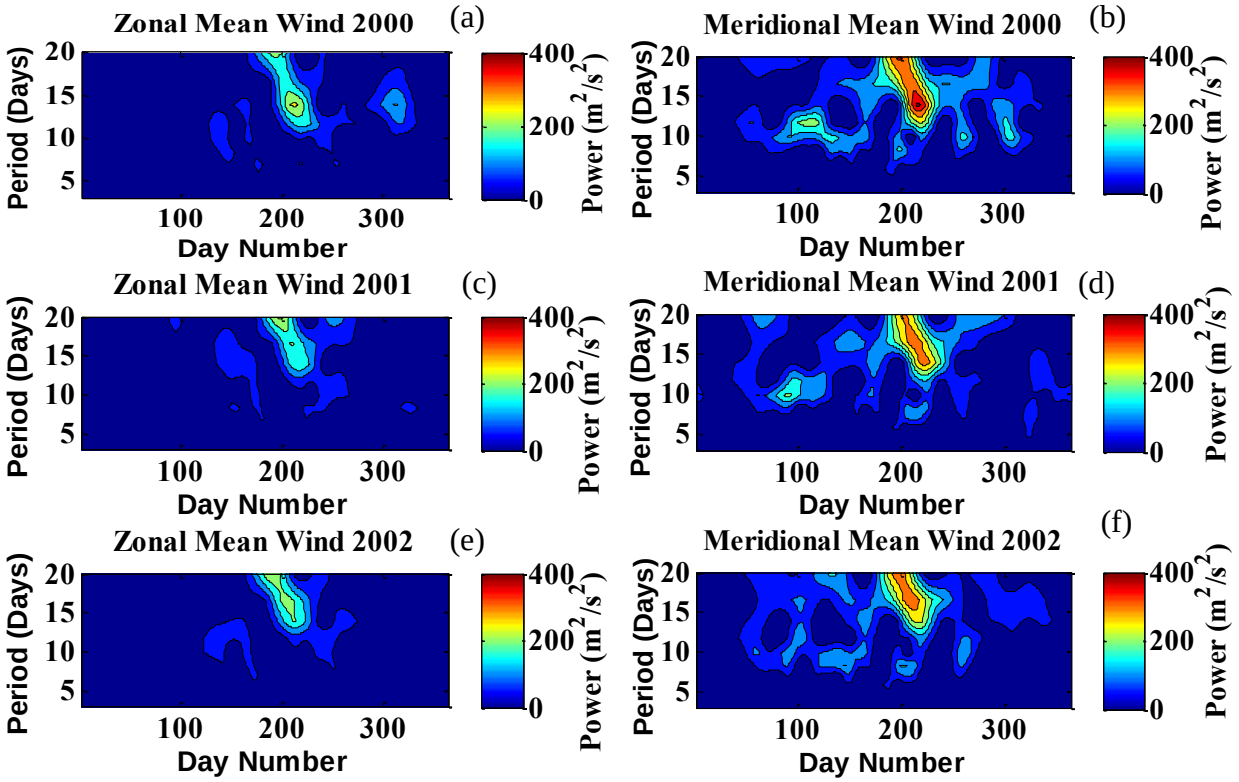

Figure 5.4. Wavelet spectra of zonal (left column, a, c, e) and meridional (right column, b, d, f) mean winds at ~90 km from SuperDARN HF radar at Halley (68˚S, 27˚W) during 2000, 2001 and 2002.

Figs. 5.3 (left column) and 5.4 (left column) show that the wave activity for SANAE is weaker than for Halley, with a wave power of ~100 $m^2.s^{-2}$ and ~200 $m^2.s^{-2}$, respectively. Also, Figs. 5.3 (right column) and 5.4 (right column) show that the meridional mean wind for SANAE is weaker than the meridional mean wind for Halley. Most of the wave activity at the Halley site occurred in winter, while at SANAE most wave activity occurred in summer and winter.

The main forcing of longer period travelling waves in winter at mesospheric heights (see Figs. 5.3 & 5.4) was an internal variability of the quasi stationary planetary waves in the stratosphere (Fedulina et al., 2004; Chshyolkova et al., 2006). Moreover, the significant activity of eastward propagating waves in the southern hemisphere was associated with the seasonal changes of the general circulation of the middle atmosphere (Liu and Roble, 2005). The results observed in this study are consistent with the findings of the above authors.

5.3 The quasi 2-day wave

The zonal and meridional mean wind data measured at SANAE and Halley for the years 1997 to 2007 were used to determine the characteristics of a quasi 2-day wave. The dominant spectrum components of a quasi-2-day wave were investigated, using the spectral analysis method. The aim of this section is to investigate the quasi 2-day wave for the zonal and meridional mean wind components.

Planetary waves with periods of 1.5 to 3.5 days and zonal/meridional wavenumbers of up to 5 were investigated. The main purpose was not only to define the predominant periods of the wave components that contributed to the variability of the atmospheric fields, but also to isolate and study them in detail. The wavelet analysis and STFT techniques were used.

Figure 5.5 presents the wavelet analysis of the zonal and meridional normalised power spectrums at SANAE and Halley for the year 2002. In this chapter, three dominant spectra are identified and studied, namely, 2-, 2.5-, and 3-day waves. A wave fluctuating from 1.5 to 3.5 days is assumed to be a QTDW (quasi 2-day wave). The 2.5-day wave is clearly evident in summer and winter at both stations, particularly at Halley (see Figs. 5.5 (c) & (d)).

The diurnal tide was observed at both stations for the zonal and meridional normalised power spectrum. Tides change with the seasons. For instance, the diurnal tide is mostly seen between day numbers ~100 and ~250 for the zonal and meridional normalised power spectrum at Halley (see Figs. 5.5 (c) & (d)), while the diurnal tide is stronger between day numbers ~50 and ~300 at SANAE (see Figs. 5.5 (a) & (b)). Most of these tides were observed in the winter and summer months and their amplitudes vary with the respective seasons.

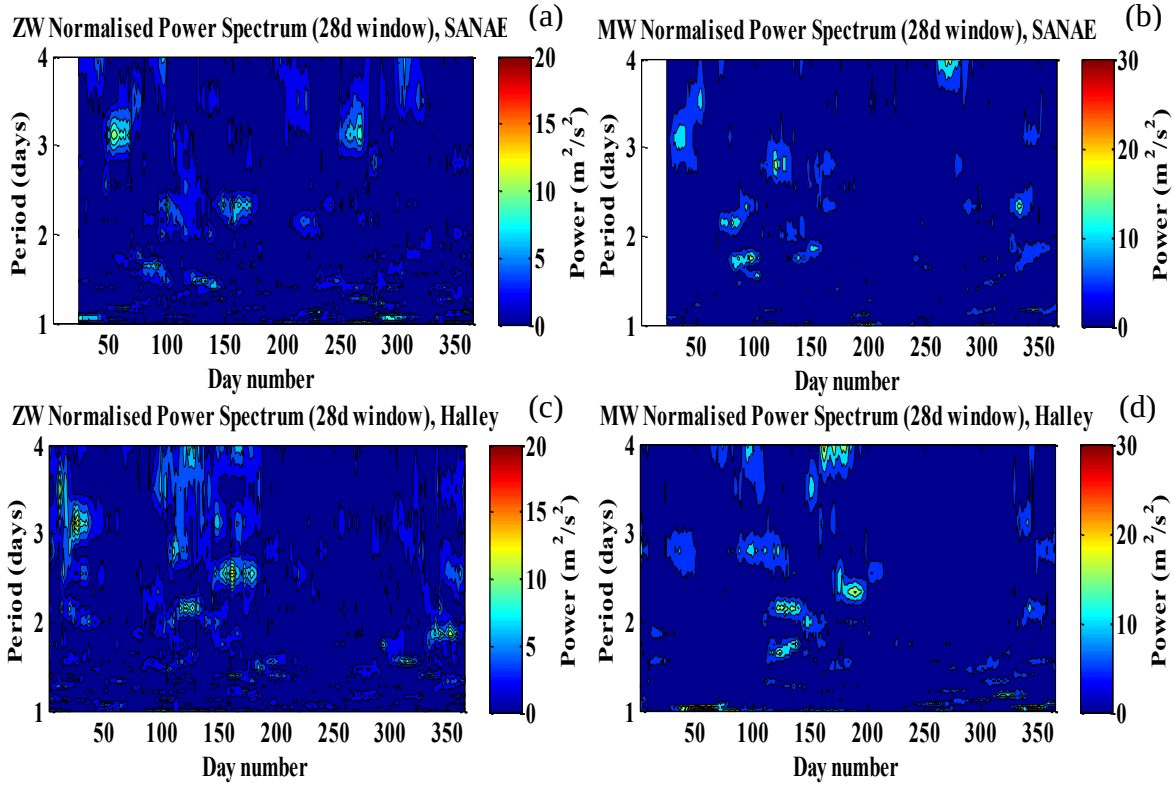

Figure 5.5. The normalised power spectra for the zonal and meridional flow over Halley and SANAE stations in 2002. The zonal and meridional normalised power spectra are represented by (a), (b), (c) and (d) over Halley and SANAE stations, respectively.

Fig. 5.6 shows the normalised Fourier power spectra of the QTDW for the zonal (a, c) and meridional (b, d) wind components. The horizontal line represents the 95% confidence level. Fig. 5.6 shows a clear seasonal variation in the wave activity of the zonal and meridional normalised power spectra. The QTDW is mostly above the confidence level in summer and winter. Strong wave peaks appear around day numbers 100-150 (wave amplitude of ~15 $m^2.s^{-2}$) for the zonal

normalised power (see Figs. 5.6 (a) & (c)), while for the meridional normalised power spectrum (see Figs. 5.6 (b) & (d)), strong wave peaks are observed around day numbers 150-200 (wave amplitude of ~20 $m^2.s^{-2}$). The strongest wave power for both the meridional and zonal normalised power at both stations is a 2.5-day wave.

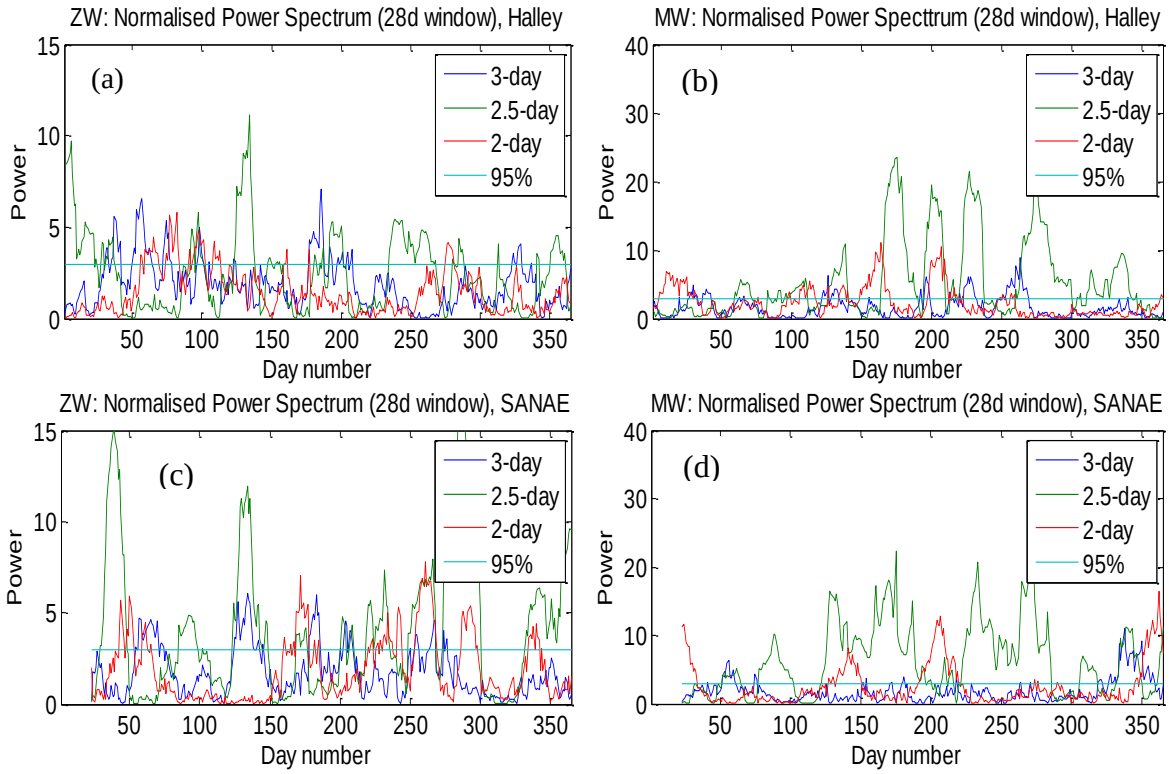

Figure 5.6. The normalised power spectra of the zonal and meridional (2-, 2.5-, 3-day) QTDW components over Halley (a) & (b) and SANAE (c) & (d) stations. The horizontal line represents the 95% confidence level.

5.4 The QTDW power and the mean flow

The objective of this section is to investigate the correlation between the meridional power spectra and the wind components (zonal and meridional wind) mean flow as shown in Fig. 5.7. For both stations, there are instances where the amplified meridional power correlates with a northward acceleration of the meridional mean flow (see Figs. 5.7 (b) & (d)), while the meridional power and the zonal mean flow (see Figs. 5.7 (a) & (c)) show a westward acceleration during amplified wave activity at both stations.

The amplitudes of 5 m.s^{-1} for the meridional peak power correspond with the northward/eastward acceleration of the zonal and meridional mean flow for both stations. A similar study was done by Malinga and Ruohoniemi (2007) for the Northern hemisphere. They found that meridional power coincides with the westward acceleration of the zonal mean flow and the meridional power enhancement tends to correspond with strong southward meridional mean flow. These results are consistent with their results.

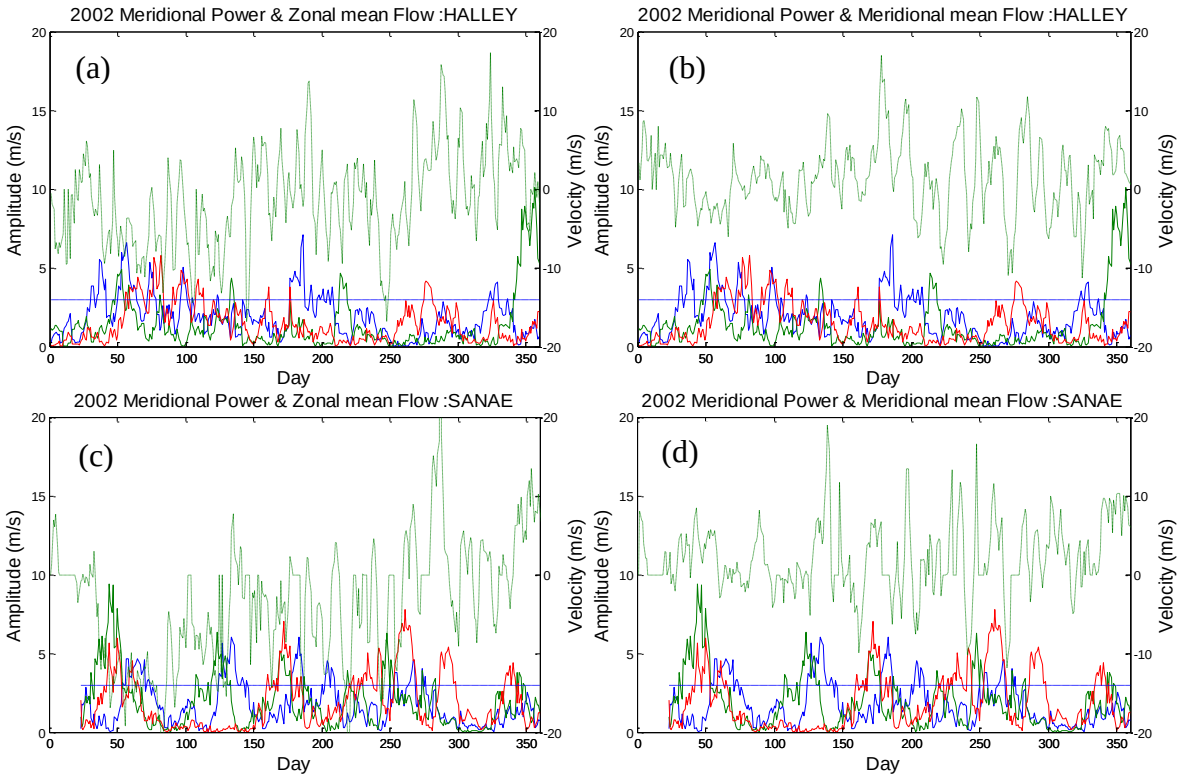

Figure 5.7. The normalised power spectra of the meridional 3- (blue), 2.5- (green) and 2- (red) QTDW components. The zonal mean flow is represented by a green dotted line in all four graphs. The horizontal line shows the 95% confidence level. The meridional power and zonal or meridional mean flow is represented by (a) or (b) and (c) or (d), respectively.

5.5 Zonal wavenumber

The zonal and meridional winds were used to study the wavenumbers for the year 2002. The wavenumbers were derived from the slope of the linear regression of the quasi 10- and 14-day wave phases as a function of longitude. The zonal and meridional wavenumbers were extracted using the 28-day window Fourier analysis method.

The focus was on the winter months (day numbers 100-200) for both the meridional and zonal power spectra. The amplitude is above the 95% confidence in the winter months. The westward and eastward directions are represented by the negative and positive signs, respectively. Figs. 5.8 & 5.9 show the wavenumbers for the respective zonal and meridional wind components.

The quasi 10-day wave component is dominated by zonal wavenumbers $k = -2$ and $k = 2 \& 5$ (see Fig. 5.8 (a)), while the quasi 14-day wave component is dominated by zonal wavenumbers $k = -5, -4 \& -3$ and $k = 3 \& 5$ (see Fig. 5.8 (b)). The quasi 10- and 14-day wave components are dominated by zonal wavenumbers $k = -2$ and $k = 3$, respectively. There are other zonal wavenumbers such as $k = -3 \& -1$ and $k = 3 \& 4$, $k = -2$ and $k = 4$ that are not dominant in the quasi 10- and 14-day wave components.

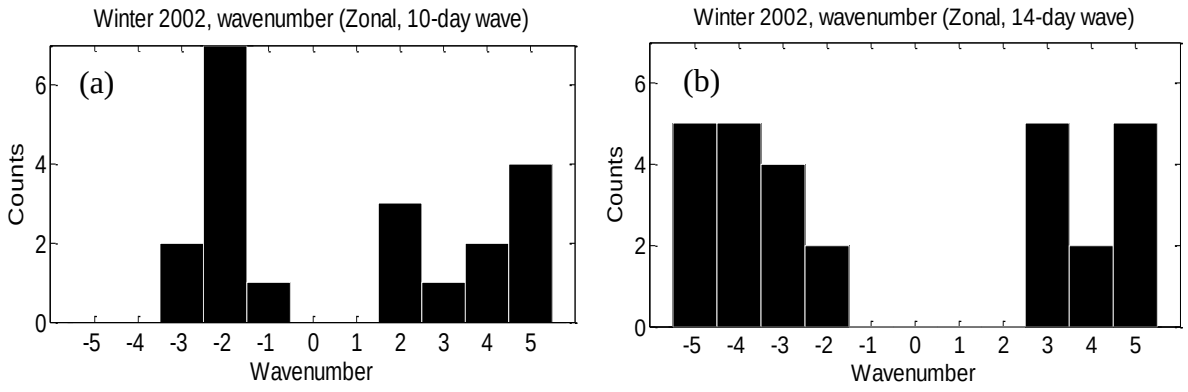

Figure 5.8. The zonal wavenumber distribution for the winter zonal quasi (a) 10- and (b) 14-day wave components in the Southern hemisphere at high latitudes. Positive and negative signs represent the eastward and westward propagating waves, respectively. The amplitudes used are greater than or equal to 2 $m.s^{-1}$.

The meridional wavenumbers as shown in Fig. 5.9 were studied. These plots show the dominant wavenumbers e.g. $k = -5 \& -3$ and $k = 4 \& 5$ (see Fig. 5.9 (a)) and $k = 2,3 \& 4$ (see Fig. 5.9 (b)) for the quasi 10- and 14-day wave components, respectively. The dominant meridional wavenumber is $k = 4$ for both quasi 10-and 14-day waves. There are other meridional wavenumbers such as $k = -4 \& -3$ and $k = 1,2 \& 3$, $k = -5,-4,-3,-2 \& -1$ and $k = 0 \& 5$ that are not dominant for both the quasi 10- and 14-day wave components. In summary, the dominant zonal and meridional wavenumbers are $k = -2$ (quasi 10-day wave) and $k = 4$ (quasi 14-day wave), respectively.

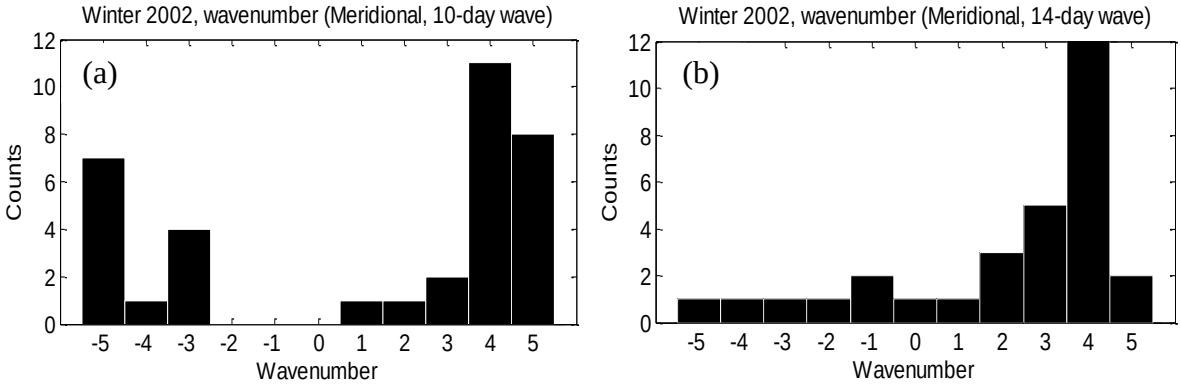

Figure 5.9. The meridional wavenumber distribution for the winter meridional (a) 10- and (b) 14 day wave components in the Southern hemisphere at high latitudes. Positive and negative signs represent northward and southward propagating waves, respectively. The amplitudes used are greater than or equal to 3 $m.s^{-1}$.

5.6 Discussion and Conclusions

Wave periods of 2-20 days were observed at Halley (76˚S, 27˚W) and SANAE (72˚S, 3˚W) in the Southern hemisphere in 2000-2002, using SuperDARN HF radars. The wavelet analysis and STFT techniques were used.

Authors like Baldwin et al. (2003) had observed mesospheric jet reversal above Antarctica prior to the unprecedented major SSW in the SH (Southern Hemisphere) in 2002. Mostly, they associated these changes in the mesosphere with the GW (gravity waves) and PW (planetary waves) forcing (see Figs. 5.2 (e) & (f)). Hoffmann et al. (2010) also studied the seasonal

variation of mesospheric waves at northern middle and high latitudes. Their findings were consistent with the filtering of westward to eastward gravity waves by the mean zonal wind.

Figs. 5.3 and 5.4 show the seasonal behaviour of the wave activity in the MLT region at both stations. Most planetary wave activity is evident for winter at Halley, while at SANAE most planetary wave activity is evident for summer. The wave power is stronger at Halley than at SANAE. For the southern hemisphere, eastward propagating waves (see Figs. 5.9 (a) & (b) and Fig. 5.8 (b)) and sometimes westward propagating waves are dominant (see Fig 5.8 (a)). Fedulina et al. (2004) suggested that the main forcing of the longer period travelling waves was an internal variability of the quasi stationary planetary waves in the stratosphere. These authors also linked the significant activity of eastward propagating waves in the southern hemisphere to the seasonal changes of the general circulation of the middle atmosphere. Many authors have shown that in the southern hemisphere an increase in the eastward propagating wave activity of the 15-day wave of wave number $k = 2$ is associated with the changes of stationary planetary waves during the seasonal transitions often seen in late winter (New and Nash, 2004; Hoffmann et al., 2010; Yamashita et al., 2010).

SuperDARN radars were used to study the behaviour of the QTDW in the Southern hemisphere for the year 2002. Many authors had studied the quasi 2-day wave before and had found that the QTDW was the strongest wave in the MLT region (Malinga and Ruohoniemi, 2007; Salby and Callaghan, 2000; Tunbridge and Mitchell, 2009). Figs. 5.5 & 5.6 show the results of the quasi 2.5-day wave observations for winter or summer at both stations. The amplitudes of these waves are >5 $m^2.s^{-2}$ and >10 $m^2.s^{-2}$ on day numbers 100-150 and 150-200 for the zonal and meridional normalised power spectra, respectively.

Tunbridge and Mitchell (2009) observed similar behaviour for planetary wave activity with amplitudes exceeding 10 $m.s^{-1}$ during winter and summer. The authors suggested that the winter 2-day wave amplitudes may be due to nonlinear coupling process between the 2-day wave and other waves such as planetary waves and tides. During summer the 2-day wave may be caused by instabilities associated with summer mesospheric jet. The seasonal behaviour of the 2-day wave suggests that it interacts with mean winds in winter.

The amplified wave activity of the meridional wave power correlate with the westward acceleration of the zonal mean flow, as shown in Figs. 5.7 (a) and (c). Also, the meridional power enhancement corresponds with the strong northward meridional mean flow, as shown in Figs. 5.7 (b) and (d). A similar study was done in the Northern hemisphere by Malinga and Ruohoniemi (2007). They found that the meridional power coincides with the westward acceleration of the zonal mean flow and that meridional power enhancement tends to correspond with strong southward meridional mean flow.

The observation of long period planetary waves having short wavenumbers during the winter season agrees with the observations of Pancheva et al. (2008). The winter season is often dominated by planetary wave activity of quasi 10- and 14-day waves with zonal wavenumbers ($k = \pm 3$) for both zonal and meridional wind components (Chshyolkova et al., 2006). The 10- and 14-day waves show seasonal variations in enhanced wave activity for winter and summer (Figs. 5.3 and 5.4). Salby and Callaghan (2000) suggested that the enhancement in wave activity could be linked to baroclinic instabilities, as the peak amplitude increases with the instability strength. Also, background wind changes in the atmosphere cause instability in the mean zonal wind distribution and this instability generates zonal wavenumbers 3 and 4 (Marzlyakov and Jacobi, 2004).

The dominant zonal and meridional wavenumbers of $k = -2$ (quasi 10-day wave) and $k = 4$ (quasi 14-day wave) suggest that the wide range of wavenumbers could be due to non-linear interaction between tides and short planetary waves. Lima et al. (2004) suggested that the non-linear interaction between tides and planetary waves can cause variability in the amplitude and phase of the solar tide. In this chapter, the zonal and meridional wavenumbers are similar to the wavenumbers observed at high latitudes by other authors (Baumgaertner et al., 2008; Tunbridge and Mitchell, 2009).

Chapter 6 Planetary waves coupling between the stratosphere and the mesosphere

6.1 Introduction

The dynamics of the middle atmosphere in winter are dominated by planetary waves with large amplitudes. The most important of these are the quasi-stationary Rossby waves, which propagate upward from the troposphere and are very strong but quite variable during winter. These waves have periods of ~2, 5, 10 and 16 days and do not generally transport much momentum, but can interact with other waves or the zonal mean flow. Therefore, wave-wave interactions may play a crucial role in the dynamics of the middle atmosphere and certainly contribute significantly to the variability of the population of atmospheric waves in the MLT region (Pancheva et al., 2008). Planetary waves are vital in the coupling between the layers of the atmosphere, as they act to move energy and momentum both horizontally and vertically in the atmosphere. Planetary waves are known to propagate from sources in the troposphere and stratosphere into the MLT (mesosphere and lower thermosphere) region (Charney and Drazin, 1961; Forbes et al., 1996).

The objective of this chapter is firstly to investigate the seasonal behaviour of the planetary waves in the zonal and meridional mean winds using HF radars and UKMO data from 2001 to 2003. Secondly, it is to investigate the seasonal behaviour of UKMO winds at a ~60 km altitude (0.316 hPa). Finally, this chapter aims to investigate PW (planetary wave) coupling processes in the stratosphere and mesosphere regions using UKMO assimilated data and the mesospheric wind data as provided by the SANAE and Halley SuperDARN HF radar networks in Antarctica.

6.2 Results and Discussion

The zonal and meridional wind data of the two radar stations, measured at high latitudes of between 72˚S and 76˚S at ~90 km altitude, were used. These radars have no height resolution. Wavelet analysis and STFT techniques were employed and a 4-day moving window was used to calculate the daily mean wind components. The segment was then stepped forward by 1 day

through the meridional and zonal wind time series in order to yield daily spaced values of prevailing wind.

Zonal and meridional winds were used for studying the PWs in the MLT region. The wave periods were studied by means of wavelet transform methods. The wavelet amplitudes of the HF radar wind components were calculated for a period ranging from 2 to 30 days at ~90 km altitude. The time interval covered 11 years of data (from 1997 to 2007) for better assessment of the PW activity in the southern hemisphere, and the years of interest were 2001-2003.

The contours of the amplitudes obtained over Halley were calculated. Fig. 6.1 presents the results for the zonal and meridional mean winds in the left (a, c, and e) and right (b, d, and f) columns, respectively. It can clearly be seen from these figures that the meridional winds exhibit weaker PW activity than the zonal winds. In addition, the figures show that the zonal wave enhancement does not usually coincide with that of the meridional winds. Wavelet analysis was employed in this study to investigate the character of the PW activity changes with season.

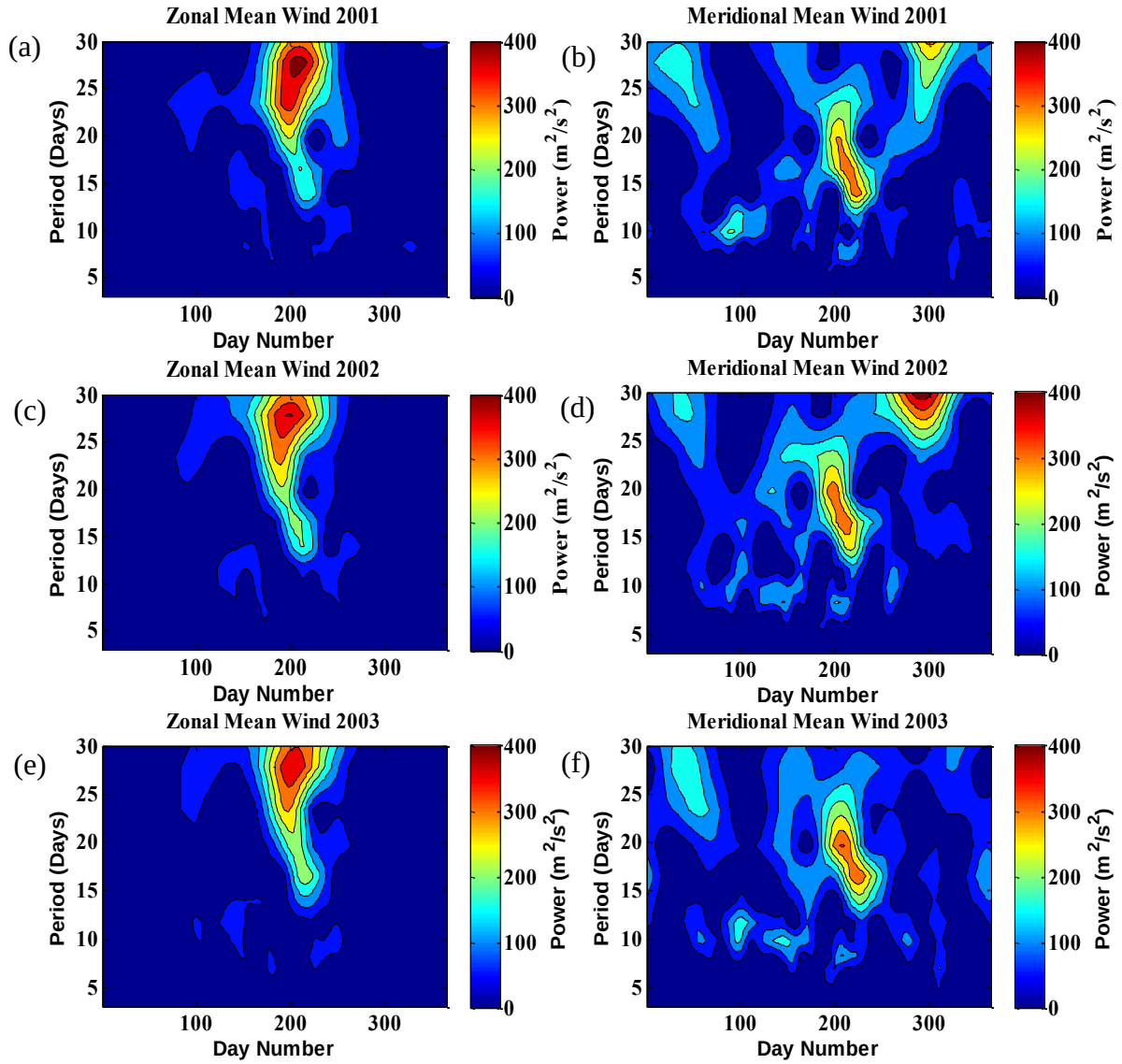

Figure 6.1. Wavelet amplitudes versus Day number calculated for the zonal and meridional mean wind components of the HF radar at ~90 km at Halley station for the years 2001-2003. The results for the zonal and meridional mean winds are presented in the left (a, c, and e) and right (b, d, and f) columns, respectively.

Strong planetary waves were observed for both wind components in winter months. These PWs are dominant between day numbers ~200 and 250. Their maximum wave power is 400 $m^2.s^{-2}$ and 600 $m^2.s^{-2}$ with wave activity lasting ~5 days for the zonal and meridional mean winds, respectively. In the zonal mean winds, Fig. 6.1 (left column) shows a strong quasi 25-30-day

wave while in the meridional mean winds, Fig. 6.1 (right column) shows a strong quasi 15-20-day wave.

Other waves in the meridional mean winds were observed during the summer and winter of 2001 and 2003. Most of these waves are quasi 10-day waves as shown in Figs. 6.1(b) and (f). Their wave power is less than 300 $m^2.s^{-2}$ with wave activity lasting ~1 day.

A study similar to the one at Halley station was done at SANAE station, Fig. 6.2 presents the results for the zonal and meridional mean winds in the left (a, c, and e) and right (b, d, and f) columns, respectively. It can clearly be seen from the plots that the meridional winds exhibit stronger PW activity than the zonal winds.

Fig. 6.2 (left column) in the zonal mean winds shows weaker wave activity with periods of ~20-day waves. However, Fig. 6.2 (right column) in the meridional winds shows strong planetary wave periods (~10-15 and ~20-25 days) for the summer months (January and December). These meridional PWs are dominant between day numbers 20-50 and 300-350. The maximum wave power is ~200 $m^2.s^{-2}$ and ~300 $m^2.s^{-2}$ for the zonal and meridional mean winds, respectively.

For the zonal mean wind, the dominant wave period is ~20-days around day number 100 for 2001 and 2002, whereas for the meridional mean wind, the dominant waves are ~11, ~25 and ~14 days for 2001, 2002 and 2003, respectively. Furthermore, the quasi 14-day wave on day number ~250 has a wave power of ~400 $m^2.s^{-2}$ and a wave activity lasting ~5 days. Fig. 6.2 (right column) shows longer periods (>10-day waves), mostly for summer at SANAE.

Additionally, Figs. 6.1 (left column) and 6.2 (left column) show that wave activity at Halley is dominant compared to SANAE with a wave power of ~400 $m^2.s^{-2}$ at Halley and ~200 $m^2.s^{-2}$ at SANAE. Also, Figs. 6.1 (right column) and 6.2 (right column) show that the meridional mean wind at SANAE is weaker than the meridional mean wind at Halley. Their wave power ranges from ~300 $m^2.s^{-2}$ and ~400 $m^2.s^{-2}$ for both SANAE and Halley. Most of the wave activity at Halley occurs in winter while at SANAE most wave activity occurs in summer and early winter. Chshyolkova et al. (2006) found that PWs have longer periods in winter than in summer at mesospheric heights.

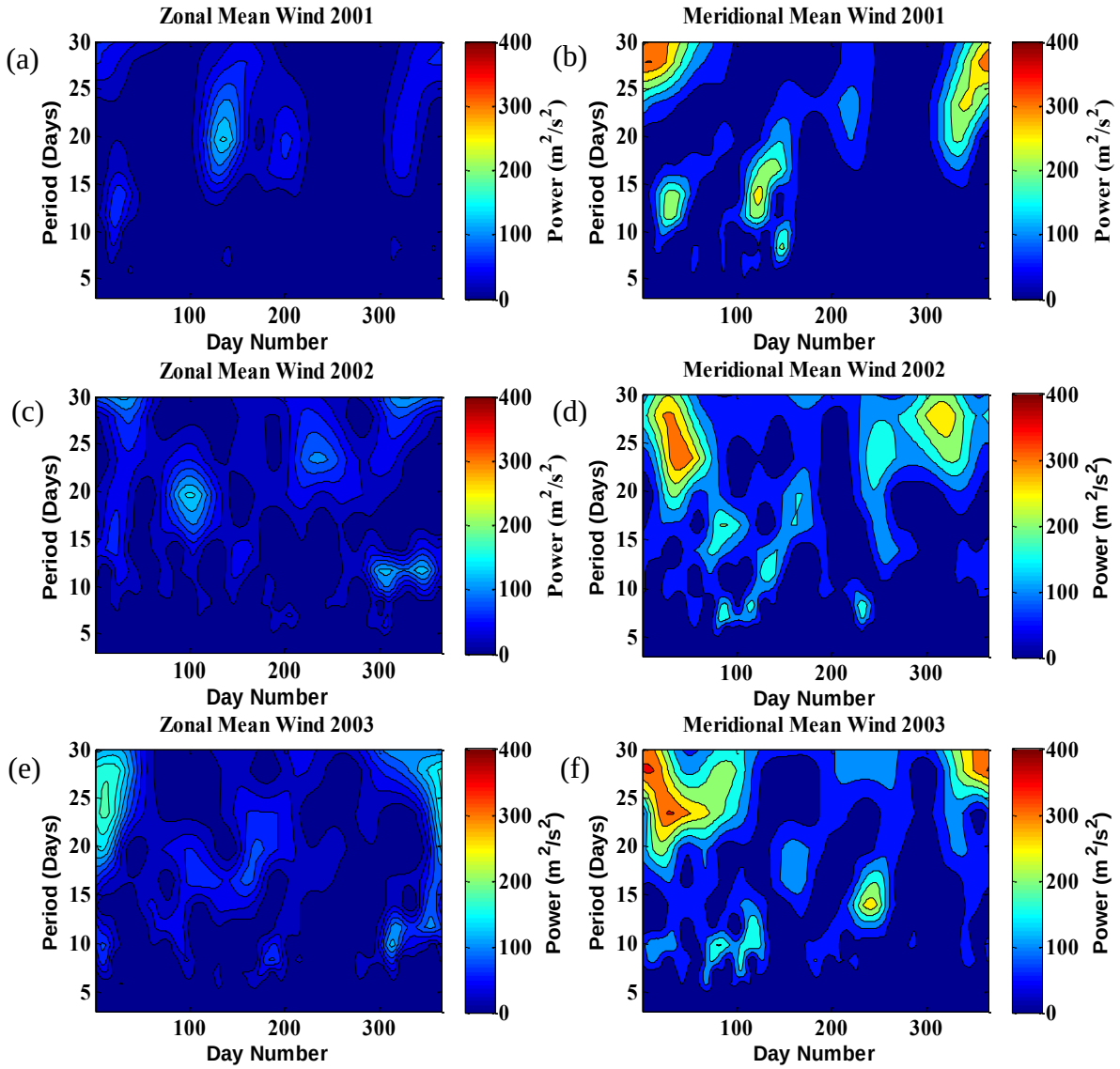

Figure 6.2. Wavelet amplitudes versus Day number calculated for the zonal and meridional mean wind components of the HF radar at ~90 km at SANAE station for the years 2001-2003. The results for the zonal and meridional mean winds are presented in the left (a, c, and e) and right (b, d, and f) columns, respectively.

Both stations results show different structures, peak occurrences and periods. The analysis of the planetary waves indicate the latitudinal dependence in the MLT, while the longitudinal distribution of the phases reveal that, at high latitude, the planetary waves of ~10-20-day periods

are dominant in the MLT (Luo et al., 2002). The results observed in this study are consistent with their findings.

This study also investigated the character of the PW activity changes with season. Fig. 6.3 shows the UKMO zonal and meridional mean wind components at 0.316-hPa (~60 km) altitude. These plots show the power spectrum wind components and cover a three years (2000-2002) time interval for and reflect the PW activity in the southern hemisphere. In this section, different graphical scales are used because of the large magnitude differences between zonal and meridional winds.

It can clearly be seen from the figures that the meridional mean winds exhibit stronger PW activity than the zonal mean winds. Furthermore, the wave peaks in the zonal mean winds do not correlate with those in the meridional mean winds, e.g. the PW activity in January/December 2000 in the zonal and meridional winds had wave periods of quasi 25 and 20 days, respectively.

Fig. 6.3 (left column) shows strong wave periods of ~20-25, ~5-15 and ~5-10 days, occurring around summer and winter months with a maximum zonal wave power of 14 $m^2.s^{-2}$. Fig. 6.3 (a) shows that the most dominant waves have periods of less than 5 days. Also, Fig. 6.3 (right column) shows the most dominant wave periods as ~6.5, ~16, and ~10 days. These dominant waves were observed on day numbers 250-300, ~250 and 200-250, respectively. Most of these waves were observed during late winter months. A noticeable observation is the appearance of a 10-day wave for both wind components as shown in Figs. 6.3 (e) & (f). Even though the zonal and meridional winds differ in terms of power, both occur at the same time in winter.

Figs. 6.1 (d) and 6.3 (f) show the ~16-day wave on day numbers ~200-250 while Figs. 6.2 (d) and 6.3 (f) show the ~10 day wave between day numbers ~100-150 and ~200-250. These results conclude that these waves might be generated in the stratosphere and propagated upwards into the MLT region. Charney and Drazin (1961) stated that the propagation of PWs from the stratosphere into the middle atmosphere depends crucially on the zonal mean flow. Also, Dowdy et al. (2004) suggested that the observation of similar waves in the lower and upper atmosphere

may indicate that these waves were generated at stratospheric heights and propagated upward into the mesosphere.

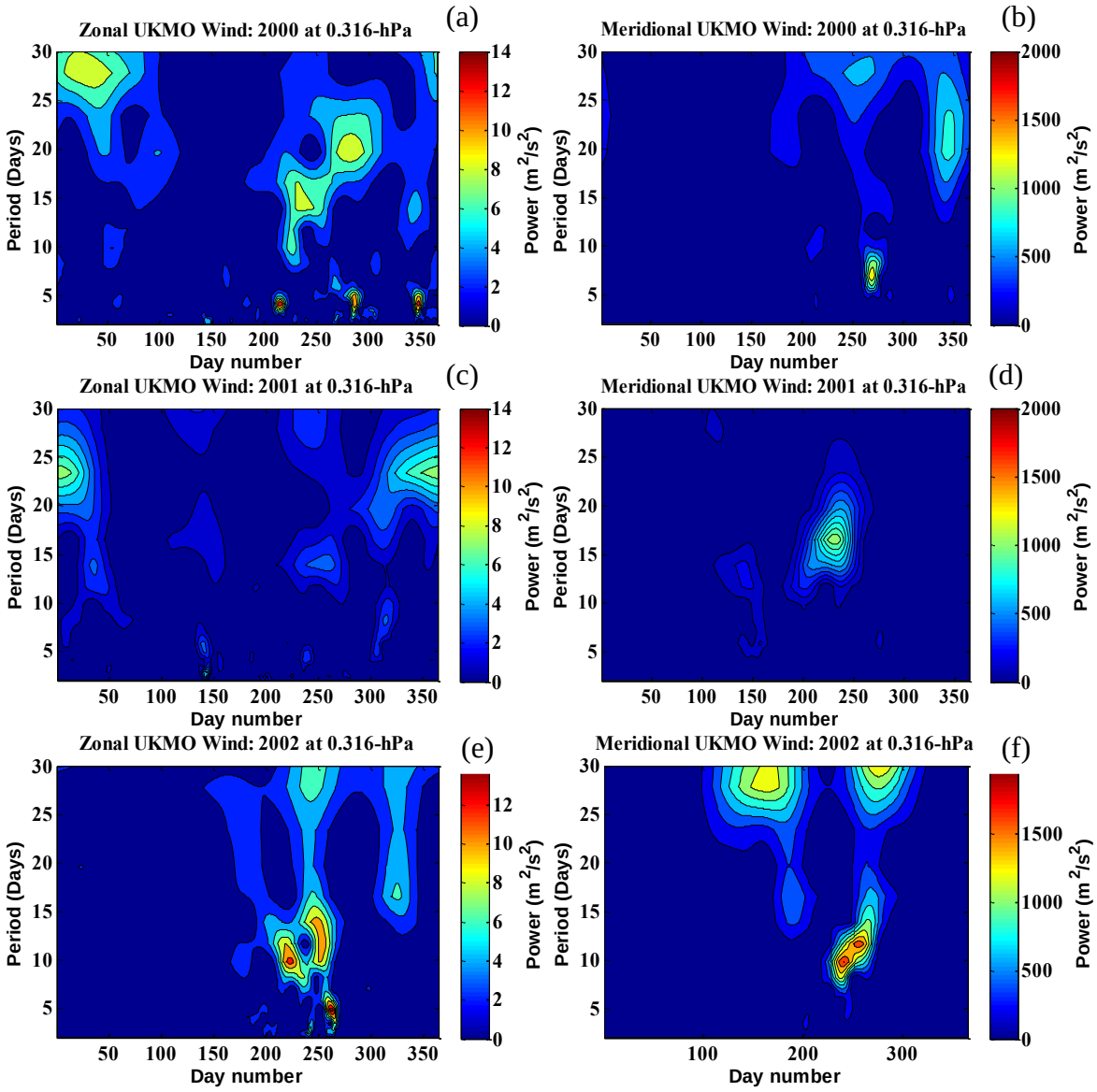

Figure 6.3. Power wave of day number vs. period (3-30 days) calculated for the zonal (a, c, e) and meridional (b, d, f) wind components of the UKMO wind (~0.316 hPa) at 71.25˚S during the years 2000-2002. The scales of these winds were chosen differently because of large magnitude differences.

The propagation of PWs from the stratosphere into the middle atmosphere depends significantly on the zonal mean flow. Only waves with phase velocities westward compared to the mean flow can propagate upward (Charney and Drazin, 1961). In this section, the state of the atmosphere was studied using UKMO assimilated data. Fig. 6.4 shows the UKMO zonal winds for 2001 (a) and 2002 (b) at 70˚S, with 2001 being a quiet year and 2002 being a disturbed year. These figures show weak wind speeds for 2001 and high wind speeds for 2002, particularly at high altitudes (10-0.316 hPa) during the winter months. For both years, the zonal mean winds show the stratospheric circulation with a strong eastward and westward flow for winter and summer, respectively.

Fig. 6.4 (b) shows the reversal of the zonal mean wind on days ~270-290 for ~10 days. Different authors have found unusually high variability in the zonal mean winds in 2002 and associated it with the major stratospheric wind (Baldwin et al., 2003; Dowdy et al., 2004; Chshyolkova et al., 2006). Moreover, Dowdy et al. (2004) showed that year 2002 was dominated by weaker zonal wind and these zonal winds increased planetary wave activity at mesospheric heights. The Dowdy et al. (2004) results regarding the occurrence of zonal wind reversal were similar to the results found in this study.

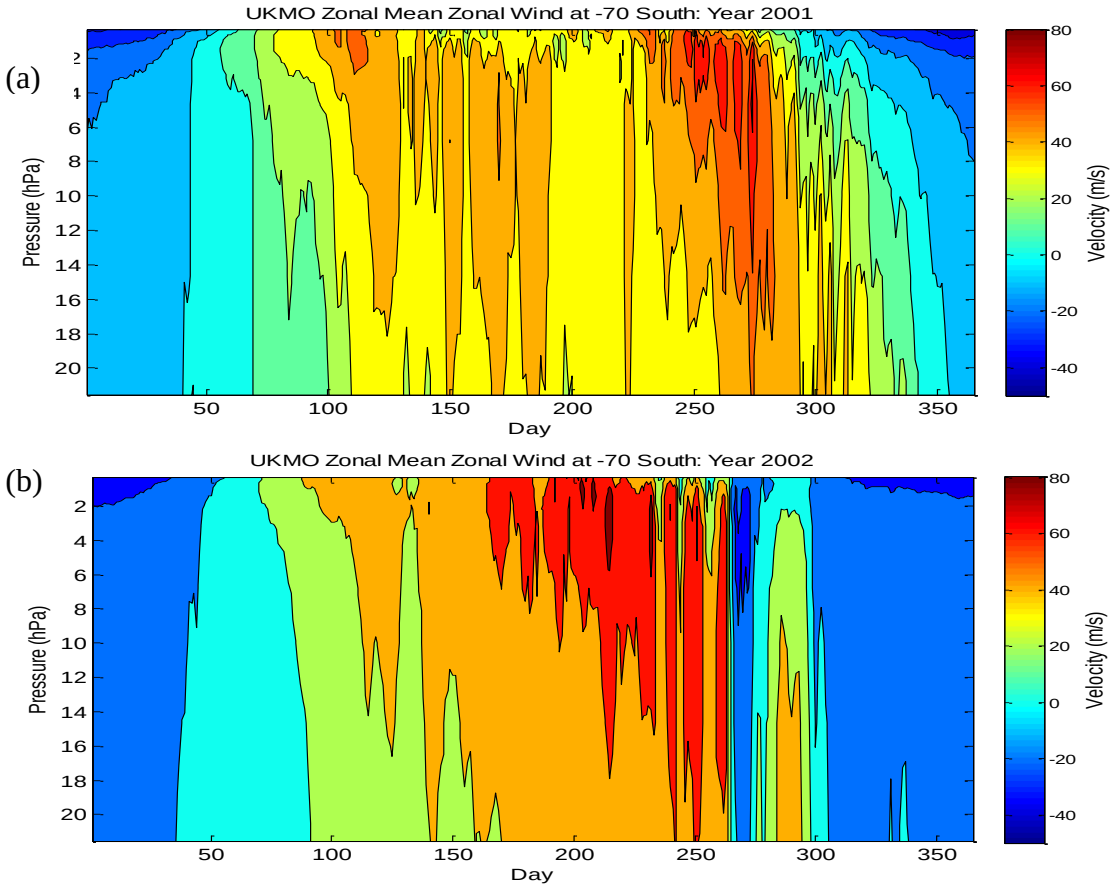

Figure 6.4. The UKMO zonal mean winds for Day number versus pressure (0.3-20hPa) at 70˚S are presented for (a) 2001 and (b) 2002.

Fig. 6.5 shows the cross power wavelet of UKMO (1-hPa) and HF (~90 km) radar winds. The aim of this study is to investigate the possibilities of the coupling between the stratospheric and mesospheric heights in the Southern hemisphere. Figs. 6.5 (a) & (b) represent the zonal and meridional mean wind components for SANAE while Figs. 6.5 (c) & (d) represent Halley. The graphical scales of these winds were chosen differently because of large magnitude differences.

Most of the planetary wave activity observed for the winter months is ~10-15 and ~20-30 days for both stations. The meridional winds (see Figs. 6.5 (b) & (d)) are stronger than the zonal winds (see Figs. 6.5 (a) & (c)). The dominant planetary waves were observed on day numbers ~150-250 and they show strong coupling between the stratosphere and mesosphere regions. During summer, a lack of planetary waves coupling was observed for both stations.

Figs. 6.5 (a) & (b) show the coupling at SANAE with visible peak power in the zonal and meridional wind components. Their wave power is ~200 $m^2.s^{-2}$ and ~300 $m^2.s^{-2}$ for the zonal and meridional wind components, respectively. Figs. 6.5 (c) & (d) show the strongest coupling at Halley with strong peak power for the zonal and meridional winds, the zonal wind being weaker than the meridional wind. The wave power is ~200 $m^2.s^{-2}$ and ~500 $m^2.s^{-2}$ for the zonal and meridional winds, respectively.

These results indicate that most of the planetary wave coupling occur in the winter months for both wind components. Fig. 6.5 (d) shows the strongest planetary wave coupling for three years (2001-2003). This is similar to a study done by Chshyolkova et al. (2006). They used 3 years' data (2000-2002) to investigate the coupling between the stratosphere and the mesosphere in the northern hemisphere. Their results proved that wave coupling occurs in winter rather than summer at most stations.

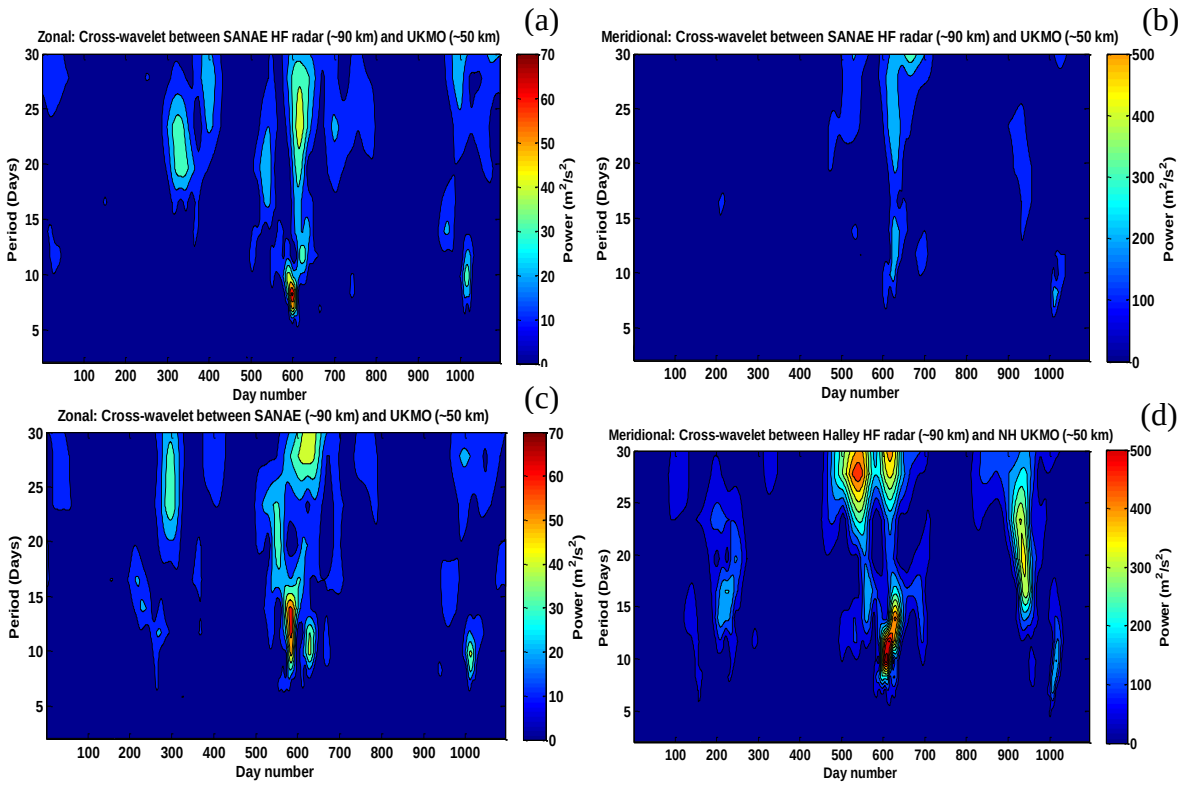

Figure 6.5. Cross wavelet power versus Day number of years 2001, 2002, and 2003 calculated between the UKMO (1-hPa) and HF radar winds (~90 km). (a) & (b) for SANAE and (c) & (d) Halley stations represent the zonal and meridional winds, respectively.

The zonal winds were used to study the zonal wavenumber for the years 2000-2002. The zonal wavenumbers were derived from the slope of the linear regression of the quasi 10-day wave phase as a function of longitude. The winter months were used to calculate wavenumbers for the dominant wave periods in three consecutive years (2000-2002). Fig 6.6 shows prominent wavenumbers for the three years under study. These months were chosen because of their strong PW activity.

Fig. 6.6 (a) represents the dominant wavenumbers for 2000 as -5,-4, -2, 2, 4 and 5. The most dominant wavenumber 4 is propagating in an eastward direction. Other wavenumbers present are -1 and 1 but they are not as dominant as wavenumber 4. These wavenumbers propagate in westward or eastward. Fig. 6.6 (b) also shows very weak wavenumbers -5, -4, -3 and 4 for 2001. This wave in 2001 is dominated by wavenumber -2 and is likely to propagate in a westward

direction. Finally, Fig. 6.6 (c) show the dominant wavenumber 1, favouring the eastward direction. The other wavenumbers that were observed (0, 2 and 3 and -5, -4 and -3) are not as dominant as wavenumber 1. The observation of longer period planetary waves (>10 days) having shorter wavenumbers during the winter season is in agreement with the observations by Pancheva et al. (2008). Notably, winter months are known for their strong planetary wave activity over a wide period (Chshyolkova et al., 2006).

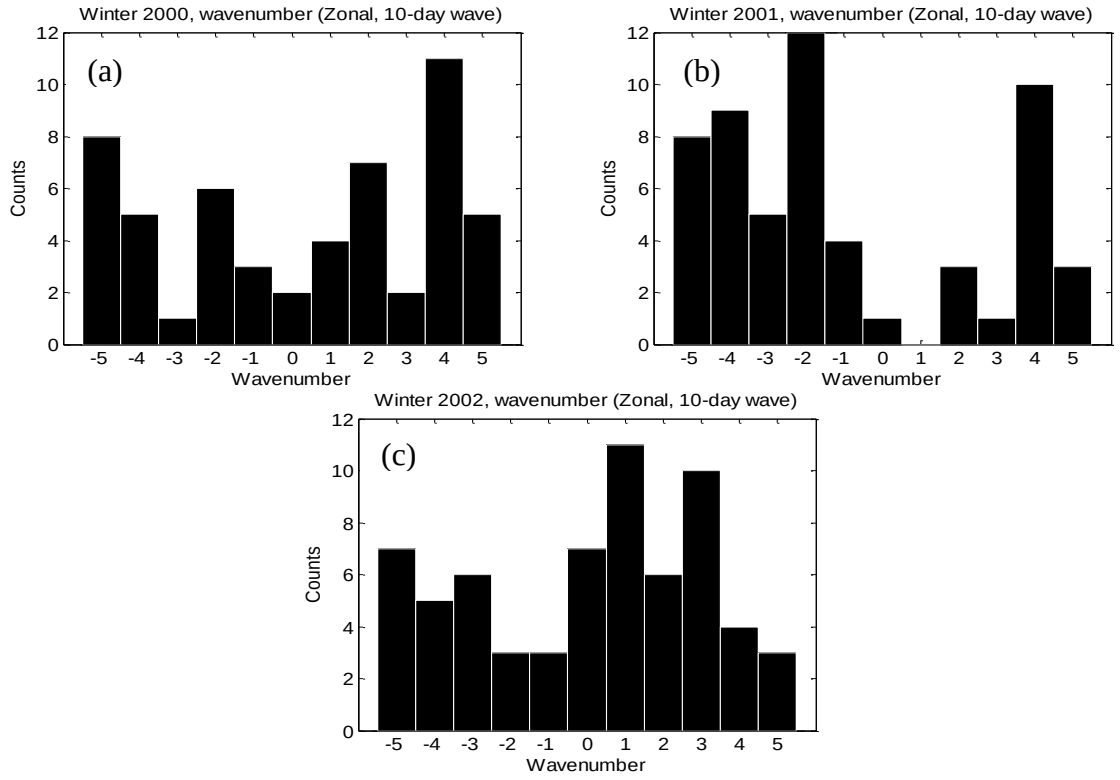

Figure 6.6. The zonal wavenumbers for the 10 day wave in three years: (a) 2000, (b) 2001, and (c) 2002 during the winter months.

6.3 Conclusions and summary

The main focus of this chapter was to study the types of PWs seen in HF radars and UKMO data and the wave coupling of the stratosphere-mesosphere region in the Southern Hemisphere for years 2000-2003. The emphasis was on the wave periods and the seasonal behaviour of the planetary waves.

The most dominant planetary waves in the zonal wind are ~25-30 days at Halley. These waves are seen on day numbers ~200-250. In the meridional winds the most dominant planetary waves are ~15-20-day period waves around the same day number as for those in the zonal wind (see Fig. 6.1). Pancheva et al. (2007) observed long period waves (23-24 day waves) in the zonal wind while the meridional wind had 15-16 day waves at almost all the stations.

However, SANAE wind components show different results from those of Halley. There are no strong peaks in the zonal wind in 2000-2003 except for 2001, where a 20-day wave was observed (see Fig. 6.2). The meridional wind shows prominent peaks in summer with periods of ~20-30 and ~10-15 day waves for all three years. The strongest peak with a ~13-day wave is seen around day number 250 (see Fig. 6. 2 (f)). This is consistent with the work done by Pancheva et al. (2008) in the MLT region, which also showed ~13-day wave periods. Fedulina et al. (2004) suggested that the forcing of the longer periods travelling waves is an internal variability of the quasi stationary planetary waves in the stratosphere.

Furthermore, in this chapter, a height of 0.316-hPa (~60 km) was selected in the UKMO data. The dominant wave peaks for the wind components were observed during winter and summer seasons. The observed wave periods are ~15-days for the years 2000-2002. The zonal amplitudes (Fig. 6.3, left column) are stronger than the meridional amplitudes (Fig. 6.3, right column). Dowdy et al. (2004) studied the dynamics of the MLT region during the SSW (sudden stratospheric warming) and found smaller amplitudes for both zonal and meridional winds. Therefore, changes in stratospheric circulation will produce changes in gravity waves filtering and these waves may propagate upwards and reach the mesosphere (Dowdy et al., 2004).

The results of the ~16-day wave (see Figs. 6.1 (d) & 6.3 (f)) and ~10-day wave (see Figs. 6.2 (d) & 6.4 (f)) suggest that these waves probably originated in the lower atmosphere and was able to propagate to the mesospheric heights, where they were detected in HF radar (~90 km) winds. These results may be attributed to the significant stationary wavenumbers observed between SANAE and Halley stations in 2002 (see Fig. 6.6 (c)). The deceleration of the mean flow in the MLT during the major SSW was linked to wavenumber 0 and 1 in the southern hemisphere (Mbatha et al., 2010b). Dowdy et al. (2004) found that the wavenumber of the ~16-day wave was westward propagating with wavenumber 1.

Fig. 6.4 shows the dominant wind components during the winter season, in particular the reversal wind in September 2002. The wind direction in 2001 and 2002 during winter season is very strongly eastward. It took more than five days for the wind to reverse in September 2002 (around days 270-290). A similar study by Dowdy et al. (2004) showed that zonal winds were weaker than usual during the 2002 winter and also during the transition to the summer circulation. Andrews et al. (1987) found that the propagation of the planetary waves from the troposphere into the stratosphere cause sudden stratospheric warmings through the changes in both planetary and gravity waves interacting with the mean flow. The changes in the filtering in the stratosphere allow gravity waves to penetrate into the MLT.

The results of the cross wavelet analysis for the UKMO (~50 km) and HF radar (~90 km) data suggest that there is strong vertical coupling between stratospheric and mesospheric heights during winter months (see Fig. 6.5). However, not all disturbances seen in the mesosphere are due to propagation from below. This result agrees with other studies that involve both the lower and middle atmosphere (Lawrence and Jarvis, 2003). Pancheva et al. (2008) investigated planetary wave coupling in the MLT region and suggested that the disturbances in the MLT region are generated by the change in the filtering in the stratosphere that allows gravity waves to penetrate into the MLT.

The phase analysis method was used to calculate the wavenumbers of the 10-day wave at both stations. The differences observed at both stations may be because of the zonal symmetry being better over shorter longitudinal (longitude difference of 24˚) distances (Dowdy et al., 2004). At

high latitudes, the longitudinal distribution of the phases reveal the strongest planetary wave to be the 10-day oscillating eastward (see Figs. 6.6 (a) & (c)) and westward waves (see Fig. 6.6 (b)) with zonal wave numbers 4, -2 and 1, respectively. In the southern hemisphere, the eastward propagating waves are associated with the seasonal changes of the general circulation of the middle atmosphere (Fedulina et al., 2004).

In summary, the analyses in this chapter have indicated that long wave periods are present in the MLT spectra. The UKMO data have shown long and short wave periods. It is worth noting that the zonal peaks are weaker than the meridional peaks, while in the UKMO data, the zonal wind is stronger than the meridional wind. The possible of coupling between the lower and upper regions was observed. The results of the wavelet analysis suggest a strong coupling between mesospheric and stratospheric heights during winter months. The wave coupling seen in the mesosphere is not all due to propagation from the stratosphere.

Chapter 7 Summary and Conclusion

This study investigated gravity wave characteristics in the middle atmosphere using imaging riometer, UKMO assimilated and HF radar data. Emphasis was put on the short-period (< 60 min.) gravity wave parameters. HF radar and UKMO data were also used to study planetary waves with a range of 2-30 days in the stratosphere and mesosphere region. The major aim was to identify the prevailing planetary waves from both the HF radar and UKMO data and study the coupling between the stratosphere and mesosphere for the years 2000-2003. The FFT and wavelet analysis methods were used to study atmospheric waves. The three main chapters of the study are summarised below.

Chapter four presented the study of atmospheric gravity waves using data from an imaging riometer. Atmospheric gravity waves play an important role in the dynamics of the mesosphere. An imaging riometer was used to obtain an understanding of the short period mesospheric gravity waves over SANAE, Antarctica. This study provides the seasonal investigation of the gravity wave parameters at high latitudes. The variation of gravity wave parameters, observed periods, wave directions, horizontal phase velocities and horizontal wavelengths were observed.

Wave propagation directions observed during the different seasons of 2000 show strong seasonal variability with a north-eastward direction. The gravity wave parameters are studied over four months: April, June, September and December; representing autumn, winter, spring and summer, respectively. The main gravity wave characteristics are horizontal wavelengths, observed periods and horizontal phase velocities, and range from 10 to 100 km, 5 to 60 min, 5 to 60 $m.s^{-1}$, respectively. These characteristics are in the same range as those observed by other authors at high latitudes (Bageston et al., 2009; Nielsen et al., 2009).

A similar study was done by Pragati et al. (2010) where they investigated the characteristics of small scale gravity waves in the mesosphere region at Allahabad in India. The observed periods, horizontal wavelengths and phase speeds of gravity waves were 5-17 min, 10-37 km and 10-48

$m.s^{-1}$, respectively. The propagation directions were north and north-eastward for April and May and showed a south-westward motion for February and March.

This study has found that the UKMO zonal wind at middle altitudes (~60 km) is very strong with a speed of ~40-60 $m.s^{-1}$ in spring. HF radar shows low velocity variations at ~90 km at a speed of ± 10 $m.s^{-1}$ throughout the seasons. The wave propagating direction is mostly eastward throughout the seasons. Stockwell and Lowe (2001) used airglow imaging and wind model (HWM-93) to study critical layer filtering of gravity waves. Their results indicated that gravity waves propagate upward where they undergo a selection process, owing to the effect of the background winds. The results also showed that the zonal wind propagates eastward for the summer while for the winter, zonal wind propagates westward. A study by Shiokawa et al. (2009) suggested that the propagation directions in the mesopause region are controlled by wind filtering, ducting processes and the relative location to the wave sources in the troposphere.

Chapter five presented the study of the planetary wave using data from the Halley and SANAE SuperDARN HF radars in the southern hemisphere at high latitudes. The study used data for the years 2000-2003 and the periods of interest were 2-30 days. Figs. 5.3 and 5.4 show strong meridional wind in winter (SANAE and Halley) with 5-, 10- and 15-day waves dominating. The seasonal behaviour of planetary waves in the southern hemisphere is often caused by baroclinic instabilities of summer easterlies (Salby and Callaghan, 2000). In another study, Fedulina et al. (2004) also suggested that the main forcing of the longer periods travelling waves is an internal variability of the quasi stationary planetary waves in the stratosphere.

The SuperDARN HF radar was used to study the quasi 2-day wave. This wave appears around winter in the zonal wind at Halley and around summer in the meridional wind at SANAE (see Figs. 5.5 & 5.6). The relationship between the QTWD and the mean flow was determined. In general, the amplified meridional power correlates with a northward acceleration of the meridional mean flow (see Figs. 5.7 (b) & (d)), while the meridional power and the zonal mean flow (see Figs. 5.7 (a) & (c)) show a westward acceleration for both stations during amplified wave activity. A similar study was done by Malinga and Ruohoniemi (2007) for the Northern hemisphere. They found that meridional power coincides with the westward acceleration of the

zonal mean flow and the meridional power enhancement tends to correspond with a strong southward meridional mean flow.

Chapter six presented the investigation of the coupling between the stratosphere and mesosphere. UKMO assimilated and HF radar data were used to investigate the coupling wave for the duration 2000-2003. The emphasis of this chapter was on the seasonal changes of planetary wave coupling in the atmosphere. It was found that most of the longer period planetary waves such as ~5-20 days occur during late winter, as seen in Figs. 6.1 and 6.2. Meridional winds are mostly seen in summer with periods of ~25-30-day waves over SANAE. However, periods of ~20-25-day waves can also be seen for the zonal wind in summer.

In addition, UKMO zonal and meridional winds were studied to investigate seasonal wave activity at ~60 km (0.316-hPa). Most of this wave activity in the meridional wind occur during late winter (see Fig. 6.3). The amplitudes that appear in summer and winter for the meridional wind (~2000 $m^2.s^{-2}$) are stronger than the amplitude of ~14 $m^2.s^{-2}$ for the zonal wind. Fedulina et al. (2004) studied the seasonal, interannual and short-term variability of planetary waves in Met office stratospheric (UKMO) assimilated fields. Their results showed that longer period planetary waves have significant amplitudes in winter, while short planetary waves are observed throughout the year in the stratosphere. They suggested that the main forcing of the longer period travelling waves is an internal variability of the quasi stationary planetary waves in the stratosphere. The significant wave activity in the southern hemisphere is also linked to the seasonal changes of the general circulation of the middle atmosphere.

Also, changes in stratospheric circulation will result in changes in gravity waves filtering, causing these waves to propagate upwards and reach the mesosphere. The propagation of PWs from the stratosphere into the middle atmosphere depends significantly on the mean flow to propagate upward (Charney and Drazin, 1961). The state of the atmosphere using UKMO assimilated data is presented in Fig. 6.4. Most other studies (Alexander et al., 2010; Hofmann et al., 2010; Nielsen et al., 2009; Taylor et al., 2009; Medeiros et al., 2005, 2007; Hibbins et al., 2006; Ejiri et al., 2003; and Stockwell and Lowe, 2001) used the models and radars used in this study to access the state of the atmosphere.

Fig. 6.4 (b) reveals the reversal of the winds for September 2002 (day numbers 270-290) as reported by most previous studies, which was associated with stratospheric warming (Dowdy et al., 2004; Newman and Nash 2004; Mbatha et al., 2010b; Yamashita et al., 2010).

Fig. 6.5 shows the coupling between the stratospheric and mesospheric heights investigated in the southern hemisphere. The cross power wavelets between the UKMO assimilated data at 1-hPa (~50 km) and the mesospheric wind data at ~90 km were studied and it was found that strong coupling occur during the winter months. A study done by Chshyolkova et al. (2006) using UKMO assimilated data and mesospheric winds has shown that strong coupling between the stratosphere and mesosphere occur during winter months. These results clearly indicate that the stratosphere and mesosphere are directly interrelated by vertically propagating planetary waves. The zonal wavenumbers of the 10-day wave were calculated and it was found that the zonal wavenumbers are dominated by zonal wavenumbers 4,-2 and 1 (see Fig 6.6).

The changes in stratospheric circulation may also have contributed to these results, because changes in the atmosphere cause gravity waves filtering and these waves may propagate upwards and reach the mesosphere. Moreover, the propagation of the planetary waves depends significantly on the mean flow, so that waves from the stratosphere can propagate upward into the middle atmosphere (Charney and Drazin, 1961; Dowdy et al., 2004).

Future work

This study can be extended by incorporating more stations using imaging riometer instruments like the Halley imaging riometer, by using other techniques like least square fit to analyse data and by including other instruments such as cameras and satellites. Satellites, for instance, can be used to study the propagation characteristics of the gravity waves in the middle and high atmosphere and to estimate the source region.

An intensive study should be conducted in order to understand atmospheric dynamics, particularly the gravity wave direction, of the atmosphere at high latitudes. Amplitude data could provide valuable additional information about gravity wave activity, especially at smaller vertical wavelengths (Baumgaertner and McDonald, 2007).

This work can be extended by doing more data analysis to study interannual differences and their effects on hemispheres; by investigating the relationship between tides and planetary waves for long periods in the Southern Hemisphere as well as by studying coupling processes between the mesosphere and ionosphere.

References

Akmaev, R. A. (2001). Simulation of large scale dynamics in the mesosphere and lower thermosphere with the Doppler spread parameterisation of gravity waves. Journal of Geophysical research.

Alexander, M., Tsuda, T., & Vincent, R. (2001). Latitudinal variations observed in gravity waves with short vertical wavelengths. Journal of the atmospheric sciences.

Alexander, P., Luna, D., Llamedo, P., & de La Torre, A. (2010). A gravity waves study close to the Andes mountains in Patagonia and Antarctica with GPS radio occultation observations. Ann. Geophys.

Andrews, D. An introduction to atmospheric physics. Cambridge Univ Pr.

Andrews, D., Holton, J., & Leovy, C. (1987). Middle atmosphere dynamics. Academic Pr.

Bageston, J., Wrasse, C., Gobbi, D., Takahashi, H., & Souza, P. (2009). Observation of mesospheric gravity waves at Comandante Ferraz Antarctica Station (62 S). Ann. Geophys.

Baldwin, M., Hirooka, T., OSNeill, A., Yoden, S., Charlton, A. J., Hio, Y., et al. (2003). Major stratospheric warming in the Southern Hemisphere in 2002: Dynamical aspects of the ozone hole split. SPARC newsletter.

Batista, P., Clemesha, B., Tokumoto, A., & Lima, L. (2004). Structure of the mean winds and tides in the meteor region over Cachoeira Paulista, Brazil (22.7) and its comparison with models. Journal of atmospheric and solar-terrestrial physics.

Baumgaertner, A. J., & McDonald, A. J. (2007). A gravity wave climatology for Antarctica compiled from Challenging Minisatellite Payload/Global Positioning System (CHAMP/GPS) radio occultations. J. Geophys. Res.

Beer, T. (1974). Atmospheric waves. Legon : Adam hilger London.

Beldon, C., & Mitchell, N. (2009). Gravity waves in the mesopause region observed by meteor radar, 2: Climatologies of gravity waves in the Antarctic and Arctic. Journal of Atmospheric and Solar-Terrestrial Physics.

Bracewell, R. N. (2000). The Fourier transform and its applications. McGrawHill higher education.

Charney, J. G., & Drazin, P. G. (1961). Propagation of planetary-scale disturbances from the lower into the upper atmosphere. Journal of Geophysical Research.

Cho, Y. M., Shepherd, G. G., Won, Y. I., Sargoytchev, S., Brown, S., & Solheim, B. (2004). MLT cooling during stratospheric warming events. Geophysical Research Letters .

Chshyolkova, T., Manson, A., Meek, C., Avery, S., Thorsen, D., MacDougall, J., et al. (2006). Planetary wave coupling processes in the middle atmosphere (30-90 km): A study involving MetO and MFR data. Journal of atmospheric and solar-terrestrial physics, 353-368.

Chui, C. K. (1992). An introduction to wavelets. Academic press.

Coy, L., Siskind, D. E., Eckermann, S. D., McCormack, J. P., Allen, D. R., & Hogan, T. F. (2005). Modeling the August 2002 minor warming event. Geophysical Research Letters.

Detrick, D. L., & Rosenberg, T. J. (1990). A phased-array radiowave imager for studies of cosmic noise absorption. Radio Science.

Diettrich, J., Nott, G., Espy, P., Swenson, G., Chu, X., Taylor, M., et al. (2005). High frequency atmospheric gravity-wave properties using Fe-lidar and OH-imager observations. Geophysical Research Letters, L09801.

Donelan, M. A., Longuet-Higgins, M. S., & Turner, J. S. (1990). Nonstationary analysis of the directional properties of propagating waves. Journal of Physical Oceanography.

Dou, X., Li, T., Tang, Y., Yue, J., Nakamura, T., Xue, X., et al. (2010). Variability of gravity wave occurrence frequency and propagation direction in the upper mesosphere observed by the OH imager in Northern Colorado. Journal of Atmospheric and Solar-Terrestrial Physics.

Dowdy, A., Vincent, R., Murphy, D., Tsutsumi, M., Riggin, D., & Jarvis, M. (2004). The large-scale dynamics of the mesosphere--lower thermosphere during the Southern Hemisphere stratospheric warming of 2002. Geophysical research.

Drevin, G., & Stoker, P. (2003). Determining riometer quiet day curves 1. The matrix method. Radio Science.

Ejiri, M., Shiokawa, K., Ogawa, T., Igarashi, K., Nakamura, T., & Tsuda, T. (2003). Statistical study of short-period gravity waves in OH and OI nightglow images at two separated sites. Journal of Geophysical Research.

Espy, P., Jones, G., Swenson, G., Tang, J., & Taylor, M. (2004). Tidal modulation of the gravity-wave momentum flux in the Antarctic mesosphere. Geophysical research letters.

Fedulina, I., Pogoreltsev, A., & Vaughan, G. (2004). Seasonal, interannual and short-term variability of planetary waves in Met Office stratospheric assimilated fields. Quarterly Journal of the Royal Meteorological Society.

Forbes, J. M. (1995). Tidal and planetary waves, The upper mesosphere and lower thermosphere:a review of experiment and theory.

Fritts, D. C. (1999). Two-day wave structure and mean flow interactions by radar and high resolution doppler imager . Geophysical Research.

Fritts, D., & Alexander, M. (2003). Gravity wave dynamics and effects in the middle atmosphere. Reviews of Geophysics-Richmond Virginia then Washington.

Grandal, B., & Holtet, A. (1977). Dynamical and Chemical Coupling between the Neutral and Ionized Atmosphere.

Greenwald, R. A., Baker, K. B., Dudeney, J. R., Pinnock, M., & Jones, T. B. (1995). DARN/SuperDARN. Space Science Reviews.

Grinsted, A., Moore, J., & Jevrejeva, S. (2004). Application of the cross wavelet transform and wavelet coherence to geophysical time series. Nonlinear processes in Geophysics.

Hayashi, H. N., T. Ogawa, Y. O., Tsugawa, T., Hosokawa, K., & Saito, a. A. (2010). Large-scale traveling ionospheric disturbance observed by superDARN Hokkaido HF radar and GPS networks on 15 December 2006. Geophys. Res.

Hibbins, R., Espy, P., Jarvis, M., Riggin, D., & Fritts, D. (2006). A climatology of tides and gravity wave variance in the MLT above Rothera, Antarctica obtained by MF radar. Journal of Atmospheric and Solar-Terrestrial Physics.

Hines, C. O. (1967). A Modeling of Atmospheric Gravity Waves and Wave Drag Generated by Isotropic and Anisotropic Terrain. Journal of Atmospheric Sciences.

Hines, C., & Reddy, C. (1967). On the propagation of atmospheric gravity waves through regions of wind shear. Journal of Geophysical Research.

Hoffmann, P., Becker, E., Singer, W., & Placke, M. (2010). Seasonal variation of mesospheric waves at northern middle and high latitudes. Journal of Atmospheric and Solar-Terrestrial Physics.

Jacobi, C. (1996). On the solar cycle dependence of winds and planetary waves as seen from mid-latitude D1 LF mesopause region wind measurements. Annales Geophysicae.

Jacobi, C., Frohlich, K., Viehweg, C., Stober, G., & Kurschner, D. (2007). Midlatitude mesosphere/lower thermosphere meridional winds and temperatures measured with meteor radar. Advances in Space Research.

Jacobi, C., Muller, H. G., Pancheva, D., Mitchell, N. J., & and Naujokat, B. (2003). Response of the mesopause region dynamics to the February 2001 stratospheric warming. Atmospheric and Solar-Terrestrial Physics.

Jarvis, M., Hibbins, R., Taylor, M., & Rosenberg, T. (2003). Utilizing riometry to observe gravity waves in the sunlit mesosphere. Geophysical Research Letters, 1997.

Jenkins, B., & Jarvis, M. (1999). Mesospheric winds derived from SuperDARN HF radar meteor echoes at Halley, Antarctica. Earth planets and space.

Kato, S. (1980). Dynamics of the upper atmosphere. Advances in Earth and Planetary Sciences.

Kishore, P., Namboothiri, S., Igarashi, K., Gurubaran, S., Sridharan, S., Rajaram, R., et al. (2004). MF radar observations of 6.5-day wave in the equatorial mesosphere and lower thermosphere. Journal of atmospheric and solar-terrestrial physics.

Kshevetskii, S., & Gavrilov, N. (2005). Vertical propagation, breaking and effects of nonlinear gravity waves in the atmosphere. Journal of atmospheric and solar-terrestrial physics .

Kumar, P., & Foutoula-Georgiou, E. (1997). Wavelet analysis for geophysical applications. Reviews of Geophysics.

Lawrence, A. R., & Jarvis, M. J. (2003). Simultaneous observations of planetary waves from 30 to 220 . Journal of Atmospheric and Solar Terrestrial Physics.

Lee, D., & Yamamoto, A. (1994). Wavelet analysis: Theory and applications. Hewlett Packard journal.

Lima, L., Batista, P., Takahashi, H., & Clemesha, B. (2004). Quasi-two-day wave observed by meteor radar at 22.7° S. Journal of atmospheric and solar-terrestrial physics.

Liu, H., & Roble, R. (2005). Dynamical coupling of the stratosphere and mesosphere in the 2002 southern hemisphere major SSW. Geophysical research letters .

Lorenc, A. C., Ballard, S. P., Bell, R. S., Ingleby, N. B., Andrews, P. L., Barker, D. M., et al. (2000). The Met Office global three-dimensional variational data assimilation scheme. Quarterly Journal of the Royal Meteorological Society.

Luo, Y., Manson, A. H., Meek, C. E., Meyer, C. K., Burrage, M. D., Fritts, D. C., et al. (2002). The 16-day planetary waves: multi-MF radar observations from the arctic to equator and

comparisons with the HRDI measurements and the GSWM modelling results . Annales Geophysicae.

Malinga, S. B., Poole, L. M., & Vincent, R. A. (2004). Long term variations in the mesospheric mean flow observed at Grahamstown and Adelaide. Journal of Atmospheric and Solar-Terrestrial Physics.

Malinga, S., & Ruohoniemi, J. (2007). The quasi-two-day wave studied using the Northern Hemisphere SuperDARN HF radars. Annales Geophysicae.

Mallat, S. (1999). A wavelet tour of signal processing. Academic Pr.

Maraun, D., & Kurths, J. (2004). Cross wavelet analysis: significance testing and pitfalls. Nonlinear Processes in Geophysics.

Mayr, H., Mengel, J., Chan, K., & Huang, F. (2010). Middle atmosphere dynamics with gravity wave interactions in the numerical spectral model. Tmospheric and solar terrestrial.

Mbatha, N., Sivakumar, V., Malinga, S. B., Bencherif, H., & and Pillay, S. R. (2010b). Study on the impact of sudden stratosphere warming in the upper mesosphere-lower thermosphere regions using satellite and HF radar. Atmospheric Chemistry and Physics.

Medeiros, A., Buriti, R., Machado, E., Takahashi, H., Batista, P., Gobbi, D., et al. (2004). Comparison of gravity wave activity observed by airglow imaging at two different latitudes in Brazil. Journal of Atmospheric and Solar-Terrestrial Physics, 647-654.

Medeiros, A., Takahashi, H., Buriti, R., Fechine, J., Wrasse, C., & Gobbi, D. (2007). MLT gravity wave climatology in the South America equatorial region observed by airglow imager. Annales Geophysicae.

Medeiros, A., Takahashi, H., Buriti, R., Pinheiro, K., & Gobbi, D. (2005). Atmospheric gravity wave propagation direction observed by airglow imaging in the South American sector. Journal of Atmospheric and Solar-Terrestrial Physics, 1767-1773.

Medeiros, A., Taylor, M., Takahashi, H., Batista, P., & Gobbi, D. (2003). An investigation of gravity wave activity in the low-latitude upper mesosphere: Propagation direction and wind filtering. Journal of Geophysical Research , 4411.

Medeirous, A. F., Takahashi, H., Batista, P. P., Gobbi, D., & Taylor, M. J. (2002). Observations of atmospheric gravity waves using airglow all-sky CCD imager at Cachoeira Paulista, Brazil (23S, 45W). Geofisica International, 29-39.

Mitchell, N., & Beldon, C. (2009). Gravity waves in the mesopause region observed by meteor radar: 1. A simple measurement technique. Journal of Atmospheric and Solar-Terrestrial Physics, 866-874.

Moffat-Griffin, T., Hibbins, R., Nielsen, K., Jarvis, M., & Taylor, M. (2008). Observing mesospheric gravity waves with an imaging riometer. Journal of atmospheric and solar-terrestrial physics, 1327-1335.

Mthembu, S. (2006). An investigation of ultra low frequency pulsations using radar data and solar wind data.

Nakamura, T., Aono, T., Tsuda, T., Admiranto, A., Achmad, E., & Surant, O. (2003). Mesospheric gravity waves over a tropical convective region observed by OH airglow imaging in Indonesia. Geophysical Research Letters, 1882.

Nakamura, T., Higashikawa, A., Tsuda, T., & Matsushita, Y. (1999). Seasonal variations of gravity wave structures in OH airglow with a CCD imager at Shigaraki. Earth Planets and Space, 897-906.

Nakamura, T., Tsuda, T., Maekawa, R., Tsutsumi, M., Shiokawa, K., & Ogawa, T. (2001). Seasonal variation of gravity waves with various temporal and horizontal scales in the MLT region observed with radar and airglow imaging. Advances in Space Research, 1737-1742.

Newman, P., & Nash, E. (2004). The unusual Southern Hemisphere Stratosphere winter of 2002. Journal of the Atmospheric Sciences.

Nielsen, K., Taylor, M. J., Hibbins, R. E., & Jarvis, M. J. (2009). Climatology of short period mesospheric gravity waves over Halley. Atmospheric and Solar Terrestrial Physics, 991-1000.

Oleynikov, A. N., Sonosnovchik, D. M., Kukush, V. D., Jacobi, C., & Frohlich. (2007). Seasonal variation of space time parameters of internal gravity waves at Kharkiv. Journal of Atmospheric and Solar-Terrestrial Physics, 2257-2264.

Oleynikov, A., Jacobi, C., & Sosnovchik, D. (2005). Parameters of internal gravity waves in the mesosphere-lower thermosphere region derived from meteor radar wind measurements. Annales Geophysicae.

Palo, S. E., Forbes, J. M., Zhang, X., Russell III, J. M., Mertens, C. J., & Mlynczak, M. G. (2005). Planetary wave coupling from the stratosphere to the thermosphere during the 2002 Southern Hemisphere. Geophysical Research Letters .

Pancheva, D., Mukhtarov, P., & Andonov, B. (2009). Global structure, seasonal and interannual variability of the migrating semidiurnal tide seen in the SABER/TIMED temperatures (2002--2007). Ann. Geophys.

Pancheva, D., Mukhtarov, P., Andonov, B., & Forbes, J. (2010). Global distribution and climatological features of the 5-6-day planetary waves seen in the SABER/TIMED temperatures (2002-2007). Journal of Atmospheric and Solar-Terrestrial Physics.

Pancheva, D., Mukhtarov, P., Mitchell, N., Merzlyakov, E., Smith, A., Andonov, B., et al. (2008). Planetary waves in coupling the stratosphere and mesosphere during the major stratospheric warming in 2003/2004. J. Geophys. Res, 2003-2004.

Pragati, R., Parihar, N., Ghodpage, R., & Mukherjee, G. (2010). Characteristics of gravity waves in the upper mesosphere region observed by OH airglow imaging. Current Science, 392.

Riggin, D., Liu, H., Lieberman, R., Roble, R., Russell, J., Mertens, C., et al. (2005). Observations of the 5-day wave in the mesosphere and lower thermosphere. Journal of Atmospheric and Solar-terrestrial Physics.

Rojas, M., & Norton, W. (2007). Amplification of the 2-day wave from mutual interaction of global Rossby-gravity and local modes in the summer mesosphere. J. Geophys. Res.

Salby, M., & Callaghan, P. (2000). Seasonal amplification of the 2 day wave relationship between normal mode and instability. Journal of the Atmospheric Sciences.

Shiokawa, K., Otsuka, Y., & Ogawa, T. (2009). Propagation characteristics of nighttime mesospheric and thermospheric waves observed by optical mesosphere thermosphere imagers at middle and low latitudes. Earth, Planets and Space, 479-491.

Shiokawa, K., Otsuka, Y., Ejiri, M., Sahai, Y., Kadota, T., Ihara, C., et al. (2002). Imaging observations of the equatorward limit of midlatitude traveling ionospheric disturbances. Earth, planets and space, 57-62.

Shirley, T., & Fairbridge, W. (1997). Encyclopedia of planetary science. Springer.

Smith, A. K. (2000). Structure of the terdiurnal tide at 95 km. Geophsical research.

Stauning, P. (1984). Absorption of cosmic noise in the E-region during electron heating events. A new class of riometer absorption events. Geophysical Research Letters.

Stockwell, R., & Lowe, R. (2001). Airglow imaging of gravity waves: Critical layer filtering. Geophysical research .

Suzuki, S. a., Liu, A., Otsuka, Y., Ogawa, T., & Nakamura, T. (2009). Characteristics of equatorial gravity waves derived from mesospheric airglow imaging observations. Ann. Geophys, 1625-1629.

Suzuki, S., Shiokawa, K., Otsuka, Y., Ogawa, T., & Wilkinson, P. (2004). Statistical characteristics of gravity waves observed by an all-sky imager at Darwin, Australia. J. Geophys. Res.

Swinbank, R., & O'Neill, A. (1994). A stratosphere-troposphere data assimilation system. Weather Review.

Swinbank, R., & Ortland, D. A. (2003). Compilation of wind data for the Upper Atmosphere Research Satellite (UARS) reference atmosphere project. Journal of Geophysical Research.

Taylor, M., Pautet, P., Medeiros, A., Buriti, R., Fechine, J., Fritts, D., et al. (2009). Characteristics of mesospheric gravity waves near the magnetic equator, Brazil, during the SpreadFEx campaign. Ann. Geophys, 461-472.

Thompson, D., Baldwin, M., & Solomon, S. (2004). Stratosphere-Troposphere coupling in the southern hemisphere. Atmosphereic sciences.

Torrence, C., & Compo, G. (1998). A practical guide to wavelet analysis.

Tunbridge, V., & Mitchell, N. (2009). The two-day wave in the Antarctic and Arctic mesosphere and lower thermosphere. Atmos. Chem. Phys, 6377-6388.

Vincent, R., & Alexander, M. (2000). Gravity waves in the tropical lower stratosphere: An observational study of seasonal and interannual variability. Journal of geophysical research.

Wilson, A., & Stoker, P. (2002). Imaging riometer observations on energetic electron precipitation at SANAE IV, Antarctica. Journal of Geophysical Research, 1268.

Wu, Q., Ortland, D., Killeen, T., Roble, R., Hagan, M., Liu, H., et al. (2008). Global distribution and interannual variations of mesospheric and lower thermospheric neutral wind diurnal tide: 1. Migrating tide. Journal of Geophysical Research.

Yamashita, C., Liu, H., & Chu, X. (2010). Responses of mesosphere and lower thermosphere temperatures to gravity wave forcing during stratospheric sudden warming. Geophysical Research Letters.